Modeling of Loop Heat Pipe Thermal Performance

Inès Gabsi[1], Samah Maalej[1], Mohamed Chaker Zaghdoudi[1,*]

[1] University of Carthage, Institut National des Sciences Appliquées et de Technologie (INSAT), Laboratoire Matériaux, Mesures et Applications (MMA) LR11ES25, Centre Urbain Nord, BP N°676, 1080 Tunis, Tunisia

ARTICLE INFO	ABSTRACT
	The present work deals with the heat transfer performance of a copper-water loop heat pipe (LHP) with a flat oval evaporator in steady-state operation. Modeling the heat transfer in the evaporator was particularly studied, and the evaporation heat transfer coefficient was determined from a dimensionless correlation developed based on experimental data from the literature. The model was based on steady-state energy balance equations for each LHP component. The model results were compared to the experimental ones for various heat loads, cooling temperatures, and elevations, and a good agreement was obtained. Finally, a parametric study was conducted to show the effects of different key parameters, such as the axial conductive heat leaks between the evaporator and the compensation chamber cases, the capillary structure porosity and material, and the groove dimensions.

1. Introduction

Loop Heat Pipes (LHPs) are considered to be high heat transfer capacity passive devices that can operate at adverse tilts in the gravity field, and they can transfer heat over long distances. Due to the capillary structure in the evaporator and the compensation chamber, the LHPs possess a high capacity of pumping, and they could be solutions for thermal management in aerospace and avionic applications [1,2].

The design features and the operational characteristics of LHPs have attracted extensive interest from researchers both through experimental tests or theoretical studies. Experiments allow the classification of the LHPs into cylindrical and flat ones according to the evaporator shape. As the heat sources to be cooled have flat surfaces, LHPs with flat evaporators could fit most of them. The flat evaporators can be disk-shaped, rectangular, square, or flat-oval ones. The cylindrical evaporators could meet the flat heat source by adding flat saddles. The flat evaporators present many advantages, among which we can distinguish mainly the decrease in the thermal resistance and the weight of the evaporator; However, they also present drawbacks since the flat surface can be deformed under high vapor pressure if the heat source temperature increases accidentally. Therefore, flat evaporators should operate with vapor pressures that do not exceed the ambient pressure; otherwise, the

* Corresponding author.
E-mail address: chaker.zaghdoudi@insat.rnu.tn

evaporator thickness must be increased. This condition on the vapor pressure limits the choice of the working fluids and the range of the operating temperatures.

The location of the compensation chamber plays a crucial role in the design of the flat evaporator, and thus two kinds of technologies were developed. In the first technology, the compensation chamber is located on the side opposite to the surface being heated so that the liquid flow in the capillary wick is directed towards the heated area. They are referred to as evaporators with Opposite Side to the Compensation Chamber (OS-CC) [3-17]. Singh *et al.,* [3] investigated a copper-water LHP with a flat disk evaporator used for thermal control of computer microprocessors. They also examined the start-up reliability, the effect of the wick characteristics, and the effect of non-condensable gas on the thermal performance [4-6]. Celata *et al.,* [7] carried out a thorough experimental investigation on a copper water LHP with a flat disk evaporator. Li *et al.,* [8] reported on a copper-water compact LHP with a flat, square evaporator. The maximum heat load reached 450 W when the case temperature is below 100°C. Adoni *et al.,* [9] developed an ammonia LHP with a flat evaporator. The influence of the thermal conductance between the heater plate and the compensation chamber on the operating temperature of the LHP was investigated. Liu *et al.,* [10] carried out experimental studies on the operational characteristics of LHP with a flat evaporator by investigating the impact of different working fluids, namely methanol and acetone. Nguyen *et al.,* [11] designed a circular flat evaporator for cooling electronic devices and studied the effect of the orientation of the elevation and direction of the evaporator on heat transfer performance. Joung *et al.,* [12] developed an LHP with a flat evaporator using a specially devised vapor-liquid separator and investigated its transient response. Wang *et al.,* [13] reported on the LHP that utilizes two primary biporous wicks to reduce the impact of the leak on the compensation chamber. Xu *et al.,* [14] investigated the heat performance of a flat copper water LHP with three fill charge inventories. He *et al.,* [15] proposed a new flat evaporator structure (with OS-CC) with a strengthened ribbed plate on the side of the heating surface to surmount the distortion of the existing flat evaporator. Anand *et al.,* [16] conducted a series of experiments to investigate the effect of different working fluids on the thermal behavior of a miniature LHP with a flat evaporator with OS-CC. Zhang *et al.,* [17] developed a 3D model of an LHP with a carbon fiber capillary wick to study the steady-state inside the LHP and the effect of heat insulation layers on the heat leakage reduction in the LHP.

In the second technology, the liquid flow is directed along the evaporator wall [18-28]. They are referred to as evaporators with Aside Compensation Chamber (AS-CC). Singh *et al.,* [18] designed and tested an LHP having a rectangular evaporator with a small thickness so that it can be used in compact electronic devices. Joung *et al.,* [19] conducted a series of experiments to study the operating characteristics of an LHP using a thin planar bifacial evaporator with a bifacial wick structure for different fluid inventories. Its operating characteristics at transient and steady-state were examined [20]. Maydanik *et al.,* [21] developed a compact copper-water LHP with a flat oval evaporator. The LHP was tested in a horizontal position, and the maximum heat load reached 1174 W. Becker *et al.,* [22] fabricated a copper-water LHP with a flat oval evaporator and tested it for different LHP orientations. Zhang *et al.,* [23] conducted a series of experiments to investigate the effect of temperature oscillation on start-up behavior and thermal performance in an LHP with a flat evaporator. Wang *et al.,* [24] fabricated a copper-water LHP with a thin flat evaporator. The LHP was tested in different condenser locations and operating orientations. Choi *et al.,* [25] fabricated an LHP with sintered porous wicks used for the thermal management of high-power density desktop computers. Chernysheva *et al.,* [26] studied the effect of the orientation in the gravity field, the sink temperature, and the ambient temperature on the LHP thermal performance. Maydanik *et al.,* [27] developed a copper acetone LHP with a flat evaporator. The effect of the different orientations in the gravity field and heat sink temperature on the operating characteristics was investigated. Odagiri

and Nagano [28] developed a steady-state model of an LHP that includes liquid-vapor interface behaviors. The main research studies on OS-CC and AS-CC technologies are listed in Table 1 and Table 2.

Table 1
Summary of studies on LHPs having a flat evaporator with opposite side compensation chamber (OS-CC)

Year	Author	Evaporator shape	Evaporator dimensions	Source area	Housing material	Wick material	Working fluid	Max. heat load	Max. evaporator temp.
2007	Singh *et al.,* [3]	Flat disk	D = 30 mm t = 10 mm	7.1 cm²	Copper	Nickel	Water	70 W	100°C
2008	Singh *et al.,* [4]	Flat disk	D = 30 mm t = 10 mm	25 × 25 mm²	Copper	Nickel	Water	70 W	100°C
2009	Singh *et al.,* [5]	Flat disk	D = 30 mm t = 10 mm	25 × 15 mm²	Copper	Copper	Water	60 W	Not indicated
2010	Singh *et al.,* [6]	Flat disk	D = 30 mm t =10 mm	D = 30 mm	Copper	Copper	Water	70 W	100°C
2010	Celata *et al.,* [7]	Flat disk	D = 50 mm t = 13 mm	D = 48 mm	Copper	Stainless steel	Water	75 W	150°C
2010	Li *et al.,* [8]	Square	W = 30 mm L = 30 mm t = 15 mm	25 × 25 mm²	Copper	Copper	Water	600 W	120°C
2010	Adoni *et al.,* [9]	Flat disk	D = 150 mm t = 5 mm	D = 128 mm	Aluminum-Stainless steel	Nickel	Ammonia	300 W	43°C
2011	Liu *et al.,* [10]	Rectangular	W = 30 mm L = 40 mm t = 1.5 mm	40 × 30 mm²	Copper	Stainless steel	Methanol Acetone	60 W	55°C 52°C
2012	Nguyen *et al.,* [11]	Flat disk	D = 41 mm t = 15 mm	30 × 30 mm²	Stainless steel	Copper	Water	140 W	65°C
2013	Joung *et al.,* [12]	Rectangular	W = 52 mm L = 56.40 mm t = 5 mm	52 × 52 mm²	Stainless Steel	Stainless Steel	Methanol	140 W	120°C
2015	Wang *et al.,* [13]	Flat disk	D = 37.6 mm t = 4.3 mm	D = 36 mm	Copper	Nickel	Methanol	270 W (+ 90 °) 210 W (+ 10°)	90°C
2017	Xu *et al.,* [14]	Flat disk	D = 56 mm t = 30 mm	D = 30 mm	Copper	Copper	Water	120 W	90°C
2018	He *et al.,* [15]	Square	W = 80 mm L = 80 m T = 21 mm	54.76 cm²	Copper	Nickel	R245fa	160 W	55°C
2018	Anand *et al.,* [16]	Oval	D = 79 mm	D = 45 mm	Aluminum alloy	Nickel	Acetone Methanol Ethanol N-pentane	160W 180W 140W 120 W	60°C 63°C 67°C 43°C
2019	Zhang *et al.,* [17]	Rectangular	W=45 mm L= 47 mm t =5.3 mm	2.5 × 2.5 mm²	Copper	Carbon fiber	Water	25 W	100°C

Penerbit
Akademia Baru

Table 2
Summary of studies on LHPs having a flat evaporator with aside compensation chamber (AS-CC)

Year	Author	Evaporator shape	Evaporator dimensions	Source area	Housing material	Wick material	Working fluid	Max. heat load	Max. evaporator temp.
2007	Singh *et al.,* [18]	Rectangular	W = 35 mm L = 45mm t = 5 mm	22 × 22 mm²	Copper	Nickel	Water	50 W	98°C
2008	Joung *et al.,* [19]	Rectangular	W = 50 mm L = 54 mm t = 1 mm	50 × 50 mm²	Stainless Steel	Stainless Steel	Methyl alcohol	30 W	90°C
2010	Joung *et al.,* [20]	Rectangular	W = 52.4mm L = 56 mm t = 20 mm	50 × 50 mm²	Stainless Steel	Stainless Steel	Acetone	260 W	105°C
2011	Maydanik *et al.,* [21]	Flat oval	W = 42 mm L = 80 mm t = 7 mm	30 × 30 mm²	Copper	Copper	Water	1174 W	110°C
2011	Becker *et al.,* [22]	Flat oval	W = 42 mm L = 85 mm t = 7 mm	Not indicated	Copper	Copper	Water	100 W	85°C
2012	Zhang *et al.,* [23]	Rectangular	W = 36.5mm L = 100 mm t = 8 mm	20 × 40 mm²	Copper	Copper	Water	110 W	82°C
2012	Wang *et al.,* [24]	Rectangular	W = 36.5mm L = 100 mm t = 8 mm	20 × 40 mm²	Copper	Copper	Water	120 W	110°C
2013	Choi *et al.,* [25]	Flat disk	Not indicated	D = 30 mm	Copper	Copper - Nickel	Water	250 W	50°C
2015	Chernysheva *et al.,* [26]	Flat oval	W = 42 mm L = 80 mm t = 7 mm	30 × 30 mm²	Copper	Copper	Water	600 W	100°C
2015	Maydanik *et al.,* [27]	Rectangular	W = 42 mm L = 80 mm t = 7 mm	42 × 42 mm²	Copper	Copper	Acetone	50 W	70°C
2019	Odagiri and Nagano [28]	Rectangular	W = 68 mm L = 51 mm t = 15 mm	30 × 47.5 mm²	Stainless Steel	Stainless Steel	Acetone	280 W	100°C

In addition to the geometrical shape of the evaporator and the position of the compensation chamber, other technological aspects, namely the material of the evaporator case and the porous structure, can play an important role in the design of the LHPs. The evaporator material may be copper, which is the most used material in the literature, aluminum, or stainless steel. The material of the capillary structure also influences the thermal performance of the LHPs. Consequently, the

porous structure is made of copper, nickel, or stainless steel. The working fluids must be compatible with the materials of the LHP. The most widely used working fluid is water that is compatible with most of the materials mentioned above except for aluminum for which ammonia is used. The other fluids used are acetone, methanol, ethanol, and methyl alcohol.

Comparing the available steady-state models for LHPs with a flat evaporator, it became necessary to carry out a more refined investigation towards the development of an analytical model that could better describe LHP performance. Focusing on this matter, the proposed model of a copper-water LHP with a flat evaporator uses a different methodology than those published previously. In this steady-state model, the thermal evaporator resistance equation is solved using a correlation established from a dimensionless analysis and is expressed as a function of heat input. Nonetheless, the evaporator resistance in the existing models is fixed independently of the heat load applied. The heat leak transferred through the porous wick and the evaporator wall and the heat dissipated by evaporation at the wick-groove interface are taken into account in this model. The model was validated by comparing the experimental results found in the literature and the predicted ones. Finally, a parametric study was carried out to simulate the effects of various parameters on the LHP thermal performance.

2. Literature Survey on LHP Models and Critical Review

The thermal behavior of the LHPs is very sensitive to the operating conditions. The steady-state modeling of such systems has been the object of many researches works that have aimed to predict their operation and optimize their design. Table 3 summarizes the main studies dealing with LHP's steady-state operation. The LHP models can be divided according to the evaporator shape and the compensation chamber location. Most of which are 1D models and are based on the steady-state energy balance equations at each component of the system and the thermodynamic relationships. The main studied parameters can be classified into three groups. The first one consists of the geometrical characteristics of the LHP components, namely the depth, the width and the number of the grooves, the thickness of the wick, the length and the radius of the vapor and liquid lines, as well as the length of the condenser. The second group of parameters concerns the operating conditions, such as the heat input power, the sink and ambient temperatures, the heat exchange with the ambient, the LHP elevation, the presence of non-condensable gas, and the fill charge. The third group of parameters comprises the thermo-hydraulic properties of the capillary structure, such as the effective thermal conductivity, porosity, permeability, and the material.

Although previous studies on LHP modeling contributed significantly to the understanding of the physical phenomena involved in the operation of such systems, the literature survey evidences a lack in the modeling of the evaporation phenomenon within the capillary wick (Table 4). Indeed, many of the published models did not present details about how the evaporation thermal conductance is determined or modeled [29-47,49]. Besides, according to the literature review, to date, no models have been established for the prediction of the evaporation heat transfer coefficient in the capillary structures. Moreover, the evaporation heat transfer coefficient depends on several parameters, such as the thermal contact between the evaporator wall and the capillary wick, the wettability of the liquid, the working fluid, the heat input power, the nature of the capillary wick, and its hydrodynamic characteristics, such as porosity and permeability, and the temperature of the compensation chamber, which depends significantly on the operating conditions of the heat sink in the condenser. As such characteristics are not detailed in the published experimental studies, the evaporation thermal resistance was adjusted in the models to obtain a good agreement between the experimental results and those of the models [32,35].

Besides, some published works also considered fixed values of the evaporation thermal resistance (or thermal conductance). They are either based on the experimental results or fixed arbitrarily by considering an order of magnitude of the evaporation heat transfer coefficient [29,33,45]. Moreover, in some works, the evaporation heat transfer coefficient is determined by expressions which are not necessarily valid for the evaporation phenomenon in porous media [30,38,41,42,44].

This work aimed to contribute to the modeling of the evaporation within the capillary wick. Hence, an analytical model was proposed for which the evaporation heat transfer coefficient was determined from a correlation based on a dimensionless analysis. The coefficients of this correlation were determined from the experimental results.

Table 3
Main steady-state models on LHP

Author (year)	Model	Evaporator shape	Compensation chamber location	Studied parameters
Chuang [29] (2003)	1D	Cylindrical	AS-CC	Heat input power
Furukawa [30] (2006)	1D	Cylindrical	AS-CC	Heat input power, capillary pore radius, wick porosity, wick dimensions, vapor/liquid line length, evaporator length, and condenser dimensions
Adoni *et al.,* [31] (2007)	1D	Cylindrical	AS-CC	Heat input power and fill charge
Launay *et al.,* [32] (2008)	1D	Cylindrical	OS-CC	Working fluid, elevation, wick thermal conductivity, the temperature difference between the ambient and the heat sink
Bai *et al.,* [33] (2009)	1D	Cylindrical	AS-CC	Sink temperature, ambient temperature, elevation, nature of the wick, and working fluid inventory
Singh *et al.,* [34] (2009)	1D	Flat disk	OS-CC	Heat input power
Hamdan and Elnajjar [37] (2009)	1D	Flat	AS-CC	Pipe length, pipe diameter, condenser temperature, and heat load
Lin *et al.,* [39] (2011)	1D	Cylindrical	AS-CC	Pore size distribution (biporous and monoporous wick) and presence of vapor blanket.
Chernysheva and Maydanik [35] (2012)	3D	Flat	AS-CC	Heat input power at constant ambient-sink temperature
Chernysheva *et al.,* [36] (2013)	3D	Flat	AS-CC	Heat input power and elevation
Siedel *et al.,* [40] (2013)	2D	Flat disk	OS-CC	Evaporator heat transfer coefficient, the thermal conductivity of the liquid and vapor lines, wick thermal conductivity and its thickness, evaporator sidewall material and its thickness and insulation
Ghajar and Darabi [38] (2014)	1D	Cylindrical	OS-CC	Groove dimensions and working fluid
Bai *et al.,* [41] (2014)	1D	Cylindrical	AS-CC	Heat input power and elevation
Bai *et al.,* [42] (2015)	1D	Cylindrical	AS-CC	Elevation
Siedel *et al.,* [44] (2015)	2D	Flat disk	OS-CC	Presence of noncondensable gas and the thermal conductivity of the wick
Chernyshevaand Maydanik [45] (2016)	1D	Flat disk	OS-CC	Convective component of the heat transfer on the evaporator thermal state and heat exchange processes in the evaporation zone.

Zhu and Yu [43] (2016)	1D	Flat	OS-CC	The thickness of the wick, length of the condenser, the inner diameter of the vapor line, and the mass flow rate
Esarte *et al.,* [46] (2016)	1D	Cylindrical	AS-CC	Effect of the length and radius of the vapor lines, the wick thickness, and the condensing temperature
Weng and Leu [47] (2016)	1D	Cylindrical	AS-CC	Effect of the heat input power
Pozhilov *et al.,* [48] (2017)	3D	Cylindrical	AS-CC	The processes of evaporation in the vapor grooves
Ramasamy *et al.,* [49] (2018)	1D	Cylindrical	AS-CC	Initial flow distribution, heat load, orientation, and sink temperature
Li *et al.,* [50] (2019)	1D	Flat	OS-CC	Heat flux, surface wettability on the patterns, dynamics of the liquid-vapor interface, liquid volume fraction, temperature distribution at wick-fin, wick groove interfaces, and effective heat transfer coefficient of the evaporator.
Chernysheva and Maydanik [51] (2019)	1D	Cylindrical	AS-CC	Temperature and pressure distribution in the evaporator and pressure drop in the wick.

Table 4
Determination of the evaporation thermal resistance in the LHP models

Author (year)	Evaporation thermal resistance
Chuang *et al.,* [29] (2003)	The evaporation heat transfer coefficient is calculated from experimental data
Furukawa [30] (2006)	The evaporation thermal conductance is given by Eq. (11) (Chernysheva and Maydanik [35])
Adoni *et al.,* [31] (2007)	Not detailed
Launay *et al.,* [32] (2008)	It is adjusted to obtain good agreement between experimental and model results
Bai *et al.,* [33] (2009)	Fixed at a constant value
Singh *et al.,* [34] (2009)	Not detailed
Hamdan and Elnajjar [37] (2009)	Not detailed
Lin *et al.,* [39] (2011)	The evaporative heat transfer coefficient is calculated by Eq. (19) (Chernysheva and Maydanik [45])
Chernysheva and Maydanik [35] (2012)	The evaporation heat transfer coefficient is fixed initially and then modified by an iterative method according to Eq. (38) (Siedel *et al.,* [40])
Chernysheva *et al.,* [36] (2013)	The heat transfer in the compensation chamber is analyzed. The heat transfer coefficient is determined from Eq. (8) (Bai *et al.,* [41])
Siedel *et al.,* [40] (2013)	The evaporation heat transfer coefficient is calculated according to Eq. (45) (Weng and Leu [47])
Ghajar and Darabi [38] (2014)	The evaporative heat transfer coefficient is calculated by a micro-region model
Bai *et al.,* [41] (2014)	The evaporation heat transfer coefficient is calculated by the Fourier law of thermal conduction of liquid-saturated wick (Eq. (6) (Pozhilov *et al.,* [48])
Bai *et al.,* [42] (2015)	Not detailed
Siedel *et al.,* [44] (2015)	The evaporative heat transfer coefficient is calculated by Eq. (29) and Eq. (30) (Li *et al.,* [51])
Zhu and Yu [43] (2016)	Not detailed
Chernysheva *et al.,* [45] (2016)	The evaporation heat transfer coefficient is fixed at a constant value
Esarte *et al.,* [46] (2016)	Not detailed
Weng and Leu [47] (2016)	Not detailed
Ramasamy *et al.,* [49] (2018)	It varies with the heat load according to the values obtained from experiments

3. Description of the Modeled LHP

The model developed in this study was validated based on the experimental results of Chernysheva *et al.,* [26] as it is the only published experimental study that gives complete information and details about the geometrical characteristics of the LHP and the experimental operating conditions. Moreover, the experimental curves of the evaporator, as well as the vapor temperatures, are presented as a function of the heat load for different operating conditions, such as the heat sink temperature, the mass flow rate of the cooling water, and the tilt angle. Accordingly, it is important to recall the main LHP geometrical characteristics and the wicking structure since they are important for model development.

Chernysheva *et al.,* [26] tested a copper-water LHP with a flat oval evaporator (Figure 1(a)) measuring 80 × 42 × 7 mm. The details of the capillary structure and the grooves are shown in Figure 1(b) to Figure 1(d). The power input delivered to the evaporator is concentrated in an active zone measuring 32 × 42 mm², and the evaporator includes vapor-removal grooves, as depicted in Figure 1(b). The vapor line and the water-cooled condenser tubes have an inner diameter of 4 mm and are respectively 305 and 160 mm long. The liquid line tube has a length of 810 mm and an inner diameter equal to 3 mm. The wick is made of sintered copper powder with a pore radius of 27 μm and a porosity equal to 46 %. To ensure the cooling of the condenser, a cooling plastic jacket was used through which water is pumped [26]. The main characteristics of the LHP are indicated in Table 5.
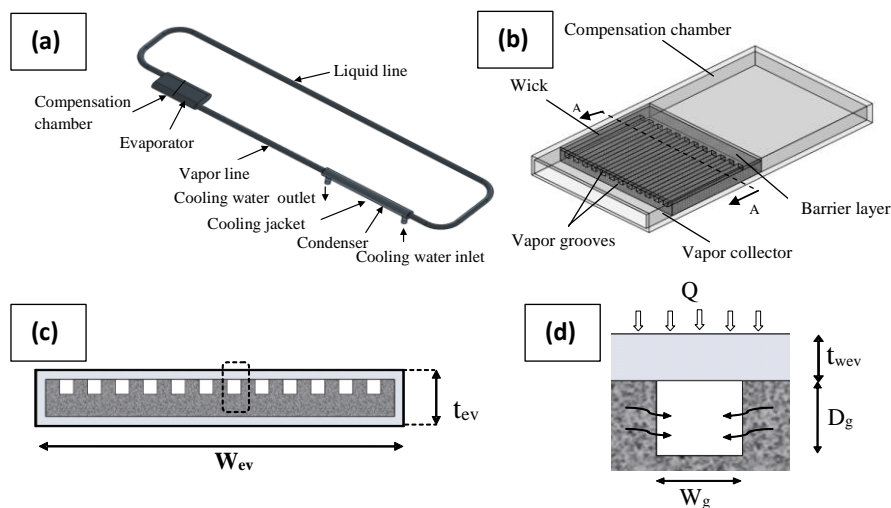

Fig. 1. General view of the copper-water loop heat pipe studied [52]: (a) General view, (b) Evaporator details, (c) Groove details, and (d) Geometrical parameters of the grooves

Table 5
Main characteristics of the modeled copper-water LHP

Evaporator	
Total length, L	80 mm
Width, W_{ev}	42 mm
Thickness, t_{ev}	7 mm
Case thickness, t_{wev}	0.5 mm
Active zone length, L_a	32 mm
Compensation chamber	
Length, L_{cc}	40 mm
Vapor-removal grooves	
Number, N_g	12
Length, L_g	33 mm
Width, W_g	1.8 mm
Depth, D_g	1.8 mm
Wick	
Wick length, L_w	33 mm
Porosity, φ_w	0.46
Pore radius, R_p	27 μm
Heating area	
Length, L_a	30 mm
Width, W_a	30 mm
Thickness, t_a	1 mm
Vapor line	
Length, L_v	305 mm
Inner diameter, D_{vi}	4 mm
Outer diameter, D_{vo}	5 mm
Liquid line	
Length, L_l	810 mm
Inner diameter, D_{li}	3 mm
Outer diameter, D_{lo}	4 mm
Condenser	
Length, L_c	160 mm
Inner diameter, D_{ci}	4 mm
Outer diameter, D_{co}	5 mm
Cooling jacket	
Inner diameter, D_{isink}	8 mm
Outer diameter, D_{osink}	11 mm
Rate of cooling water	4 ± 0.5 l/min

4. Model Description

In this section, to predict the LHP performance and optimize the geometrical parameters of the evaporator and the wick, a steady-state model will be briefly described. This analytical model is based on that developed by Gabsi *et al.,* [52]. The LHP geometry used in the model is presented in Figure 1. It includes a flat evaporator related to a compensation chamber according to AS-CC technology and connected to the heat source, a condenser to dissipate the heat load, and vapor and liquid lines to transport the working fluid between the two components. When a heat load is applied at the evaporator, the temperature rises, and the liquid vaporizes. The working fluid flows through the vapor line and reaches the condenser due to the temperature difference between the evaporator and the condenser. Then, the condensate flows toward the evaporator using the capillary wick located in the compensation chamber and the evaporator. The capillary pressure created in the core of the evaporator is responsible for the fluid circulation in the LHP. The model is based on the

equations of momentum and energy balances applied to each component of the LHP. Two thermodynamic relations enable the closing of the equation system.

4.1 Momentum Balance Equations

To ensure the circulation of the working fluid in the LHP, the capillary driving pressure generated in the capillary structure must exceed the pressure drops according to the following relationship

$$\Delta P_{cap,max} = \frac{2\,\sigma\cos(\beta)}{R_p} \geq \Delta P_g + \Delta P_{vl} + \Delta P_{ll} + \Delta P_w + \Delta P_{vg} \tag{1}$$

ΔP_{ll}, ΔP_{vl}, ΔP_w, and ΔP_{vg} are the pressure drops in the liquid line, the vapor line, the porous wick, and the vapor grooves, respectively. ΔP_g is the hydrostatic pressure drop. $\Delta P_{cap,max}$ is the maximum driving capillary pressure. The vapor and liquid pressure drops are expressed as

$$\Delta P_{vl} = F_v\, L_v Q_{in} \tag{2}$$

$$\Delta P_{ll} = F_l\, L_l Q_{in} \tag{3}$$

Q_{in} is the heat input power. F_v and F_l are the friction factors in the vapor and liquid lines, respectively. They are given by

$$F_v = 8\mu_v/(\rho_v r_v^2 A_v \Delta h_v) \tag{4}$$

$$F_l = 8\mu_l/(\rho_l\, r_l^2 A_l \Delta h_v) \tag{5}$$

A_l and A_v are respectively the cross-sections of the liquid and the vapor lines. r_l and r_v are the radius of the liquid and the vapor lines, respectively. The vapor pressure drops in the grooves, ΔP_{vg}, can be written as

$$\Delta P_{vg} = F_{vg}\, L_g Q_{in} \tag{6}$$

L_g is the groove length and F_{vg} is the friction factor in the grooves that are expressed by

$$F_{vg} = \mu_v/(K_g\, N_g\, A_g\, \Delta h_v\, \rho_v) \tag{7}$$

A_g, N_g, and K_g are the cross-section, the number, and the permeability of the grooves, respectively. The permeability of the grooves, K_g, is expressed as [6]

$$K_g = \left(D_{hg}^2\, \varphi_g\right)/(2\, P_0) \tag{8}$$

D_{hg} and φ_g are the hydraulic diameter and the porosity of the grooves, respectively. They are given by:

$$D_{hg} = \left(4D_g W_g\right)/\left(2D_g + W_g\right) \tag{9}$$

$$\varphi_g = S_g/\left(S_g + W_g\right) \tag{10}$$

The Poiseuille number, P_o, is calculated according to Gabsi *et al.,* [52]

$$P_0 = 24 \left(1 - 1.355\,\alpha + 1.947\,\alpha^2 - 1.701\,\alpha^3 + 0.956\,\alpha^4 - 0.254\,\alpha^5\right) \tag{11}$$

where

$$\alpha = \min\left(W_g/D_g\,,\,D_g/W_g\right) \tag{12}$$

The liquid pressure drops in the wick, ΔP_w, is expressed as

$$\Delta P_w = F_w\,L_w\,Q_{in} \tag{13}$$

L_w is the wick length and F_w is the friction factor in the wick written as follows

$$F_w = \mu_l/(K_w A_w \Delta h_v \rho_l) \tag{14}$$

A_w is the porous cross-section. K_w is the wick permeability which is calculated by a general correlation including the pore diameter, D_p, and the porosity of the porous medium, φ_w [52]

$$K_w = D_p{}^2 \varphi_w{}^3/(150 \times (1 - \varphi_w)^2) \tag{15}$$

The component of the gravitational force acts along the longitudinal axis. Consequently, an axial hydrostatic pressure drop is generated and is expressed as

$$\Delta P_g = \rho_v\,g\,\Delta H \tag{16}$$

The hydrostatic pressure drop depends on the elevation, ΔH, between the evaporator and the condenser. A positive elevation ($\Delta H > 0$) corresponds to the case where the condenser is placed above the evaporator, while a negative elevation ($\Delta H < 0$) corresponds to the inverse.

4.2 Thermodynamics Equations

Three different thermodynamic equilibrium states exist for each LHP component. Between these three states in the evaporator, the compensation chamber, and the condenser, the temperature variations are related to the pressure differences by the following relationships [52]

$$T_v - T_c = (\partial T/\partial P)(\Delta P_{vl} + \Delta P_{vg} + \rho_v g\,\Delta H) \tag{17}$$

$$T_c - T_{cc} = (\partial T/\partial P)(\Delta P_{ll} - \rho_l g\,\Delta H) \tag{18}$$

The slope of the saturation curve $\partial T/\partial P$ is expressed in terms of thermo-physical properties of the fluid by the Clausius-Clapeyron relationship

$$\frac{\partial T}{\partial P} = \frac{T(1/\rho_v - 1/\rho_l)}{\Delta h_v} \tag{19}$$

4.3 Energy Balance Equations
4.3.1 Energy balance equations for the evaporator section

The heat input power, Q_{in}, is transferred according to three paths. The first one is transferred to the compensation chamber, Q_{axial}, the second one is lost to the ambient, Q_{amb}, and the third one serves to the liquid evaporation within the wick, Q_{ev} (Figure 2). Hence, the energy balance at the evaporator can be written as

$$Q_{in} = Q_{axial} + Q_{amb} + Q_{ev} = G_{axw}(T_{ev} - T_{cc}) + G_{ambev}(T_{ev} - T_{amb}) + G_{ev}(T_{ev} - T_v) \qquad (20)$$

T_{ev}, T_{cc}, T_{amb}, and T_v are the evaporator, the compensation chamber, the ambient, and the vapor temperatures, respectively. G_{axw} represents the thermal conductance between the evaporator wall and the compensation chamber wall, and it can be calculated by considering expressions for heat spreading resistance as it is detailed in the study by Gabsi *et al.,* [52]. G_{ambev} represents the thermal conductance between the ambient air and the external surface of the evaporator, and it can be expressed by the classical formula for convective heat transfer mode. G_{ev} is the thermal conductance between the evaporator wall and the liquid-vapor interface within the porous wick, and it associates two thermal conductances in parallel according to

$$\frac{1}{G_{ev}} = \frac{1}{G_{wev}} + \frac{1}{G_{sp}} \qquad (21)$$

where G_{wev} is the thermal conductance that corresponds to the heat transfer by conduction through the evaporator wall, and G_{sp} is the thermal conductance due to the phase change heat transfer within the porous wick. Detailed analysis of its determination is presented in section 5.

By considering an energy balance equation, the third term in Eq. (20) can be written as

$$G_{ev}(T_{ev} - T_v) = \dot{m}\,\Delta h_v + \dot{m}\,c_{pl}(T_v - T_{cc}) + G_{cv}(T_v - T_{cc}) \qquad (22)$$

$\dot{m}$ is the mass flow rate. Δh_v and c_{pl} are the latent heat and the liquid specific heat, respectively. G_{cv} represents the conductive-convection thermal conductance.

The first term on the right of Eq. (22) is the latent heat which serves to the liquid evaporation, The second term is the sensible heat that serves to the heating of the liquid coming into the evaporator from the compensation chamber, and the third term is the heat transferred to the compensation chamber through the wick by conductive-convective heat transfer mode of which the thermal conductance is calculated according to Gabsi *et al.,* [52]

$$G_{cv} = \frac{\dot{m}\,c_{pl}}{(exp(\eta t_w - 1)} \qquad (23)$$

$\dot{m}$ is the mass flow rate and t_w is the wick thickness.

η is given by

$$\eta = \frac{\dot{m}\,c_{pl}}{(\lambda_{peff}\,A_{ev})} \qquad (24)$$

where A_{ev} is the evaporator heat transfer surface, and l_{peff} is the effective thermal conductivity which is expressed by

$$\lambda_{peff} = \lambda_p \left(\frac{2+(\lambda_l/\lambda_p)-2\, \varphi_w(1-\lambda_l/\lambda_p)}{2+(\lambda_l/\lambda_p)+\varphi_w(1-\lambda_l/\lambda_p)} \right) \tag{25}$$

λ_l and λ_p are the thermal conductivities of the liquid and the porous wick, respectively.
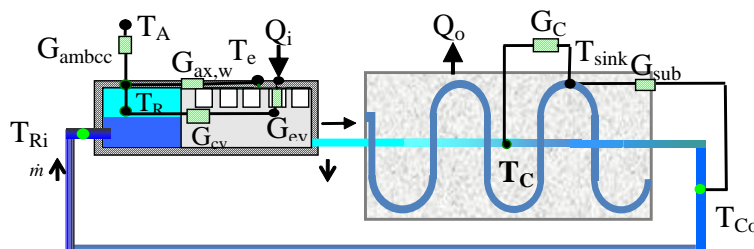

Fig. 2. LHP thermal conductance network

4.3.2 Energy balance equations for the compensation chamber

At the compensation chamber, a part of the heat flux rate, transported axially by conduction within the evaporator wall and transversally within the porous medium, is transferred by convection to the ambient, and the other part heats the liquid at the entrance of the reservoir, thus we can write

$$\dot{m}\, c_{pl}(T_{cc} - T_{cci}) + G_{ambcc}(T_{cc} - T_{amb}) = G_{axw}(T_{ev} - T_{cc}) + G_{cv}(T_v - T_{cc}) \tag{26}$$

G_{ambcc} is the thermal conductance between the compensation chamber and the ambient.

4.3.4 Energy balance equations for the condenser

The condenser can be subdivided into two zones: a condensation zone and a sub-cooled zone where the condensate is cooled under the condensation temperature. The energy balance overall the condenser can be written as

$$\dot{Q}_c = \dot{m}\, \Delta h_v + \dot{m}\, c_{pl}(T_c - T_{co}) \tag{27}$$

T_c is the condensation temperature and T_{co} is the condensate temperature at the condenser outlet. For the condensation zone, the energy balance can be written as

$$\dot{m}\, \Delta h_v = G_c(T_c - T_{sink}) \tag{28}$$

G_c is the overall thermal conductance between the condensate in the condensation zone and the heat sink, and T_{sink} is the heat sink temperature. It is expressed as the function of the condensation heat transfer coefficient, h_c, and the heat transfer coefficient between the outer condenser wall and the heat sink, h_{sink} according to

$$G_c = \frac{1}{\frac{1}{h_c\, A_{ci}} + \frac{1}{h_{sink}\, A_{co}} + \frac{1}{2\pi\, L_{cond}\, \lambda_c} \ln \frac{D_{co}}{D_{ci}}} \tag{29}$$

G_c is the thermal conductivity of the condenser wall. A_{ci} and A_{co} are the inner and outer heat transfer areas in the condensation zone, respectively. D_{co} and D_{ci} are the inner and outer diameters of the condenser, respectively. L_{cond} is the length of the condensation zone. The heat transfer coefficient, h_c, is calculated based on correlations that depend on the nature of the flow in the condensation zone. To determine the heat sink heat transfer coefficient, h_{sink}, standard Dittus-Boelter correlation is used.

For the sub-cooled zone, the energy balance is expressed as

$$\dot{m}\, c_{pl}\, (T_c - T_{co}) = \ G_{sub}\ \frac{(T_c - T_{co})}{ln\left(\frac{T_{co} - T_{sink}}{T_c - T_{sink}}\right)} \tag{30}$$

G_{sub} is the thermal conductance between the condensate and the heat sink in the sub-cooled zone. It depends on the heat transfer coefficient between the outer condenser wall and the water cooling, h_{sink}, and the heat transfer coefficient between the sub-cooled condensate and the inner condenser wall, h_{lc}. Hence, G_{sub} is expressed as

$$G_{sub} = \frac{\pi\, D_{ci}\, (L_c - L_{cond})}{\frac{1}{h_{lc}} + \frac{1}{h_{sink}}\left(\frac{D_{ci}}{D_{co}}\right) + \frac{D_{ci}}{2\pi\, \lambda_c} ln\frac{D_{co}}{D_{ci}}} \tag{31}$$

L_c is the overall condenser length. The heat transfer coefficient, h_{lc}, is calculated from classical correlations by considering laminar flow for the sub-cooled condensate.

4.3.5 Energy balance equations for the liquid line

The energy balance at the liquid line is written as

$$\dot{m}\, c_{pl}\, (T_{co} - T_{cci}) = \ G_l\ \frac{(T_{co} - T_{cci})}{ln\left(\frac{T_{co} - T_{amb}}{T_{cci} - T_{amb}}\right)} \tag{32}$$

T_{cci} is the liquid temperature at the inlet of the compensation chamber. G_l is the overall thermal conductance representing the heat transfer between the liquid and the ambient according to

$$G_l = \frac{\pi\, D_{li}\, L_l}{\frac{1}{h_{ll}} + \frac{1}{h_{amb}}\left(\frac{D_{li}}{D_{lo}}\right) + \frac{D_{li}}{2\pi\, \lambda_{wl}} ln\frac{D_{lo}}{D_{li}}} \tag{33}$$

L_{ll} is the liquid line length. D_{li} and D_{lo} are the inner and outer diameters of the liquid line, respectively. h_{ll} is the convective heat transfer coefficient between the wall and the liquid. It is calculated from classical correlations by considering the laminar flow regime.

4.4 Determination of The Operating Modes in the LHP

During normal operation of the LHP, two distinct operating modes are observed: the variable conductance operating mode (VCM) and the fixed conductance operating mode (FCM). These modes are identified by plotting the variations of the LHP operating temperature, which is generally the temperature of the compensation chamber, T_{cc}, as a function of the imposed power.

As can be seen in Figure 3, in the VCM mode, the condensation zone is short, and the condensate undergoes sub-cooling. When the heat input power increases, the operating temperature decreases.

The LHP operates in this mode when the temperature at the outlet of the condenser, T_{co}, is close to that of the heat sink, T_{sink}. This is obtained when the sub-cooling zone is large. For this mode of operation, two curve profiles represent the variations in the operating temperature, T_{cc}, as a function of Q_{in}: The U-shape or the flattened shape. The profile depends on the distribution of the heat flux rate between the evaporator and the reservoir, the heat exchanges between the sub-cooled liquid in the liquid line and the ambient, and between the compensation chamber and the ambient. The leakage heat flux rate transferred by conduction through the evaporator wall and by convection through the porous medium can also influence the profile of the curve $T_{cc} = f(Q_{in})$. The operation in fixed conductance mode (FCM) is characterized by an almost linear increase of the operating temperature with the imposed power. The variations in the operating temperature depend mainly on the heat exchanges at the condenser and are less sensitive to the distribution of the leakage heat flux rate between the evaporator and the compensation chamber.
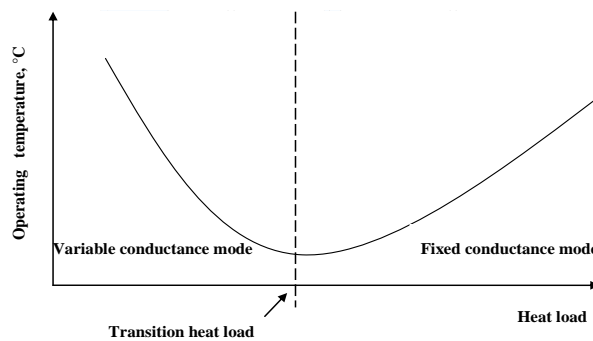
Fig. 3. The two operating modes of the LHP

To predict the thermal behavior of the LHP and facilitate the study of the influence of certain parameters, simplified equations for each mode of operation of the LHP are presented in this section and are deduced from the system of linear equations developed previously. Since the physical mechanisms acting on the LHP behavior during VCM and FCM are very different, two operating-temperature expressions of T_{cc} are proposed to describe the LHP operation [52]

$$T_{cc_{VCM}} = \frac{T_{sink} + \frac{\Delta h_v}{c_{pl}}\left[\frac{G_{axw}}{G_{ev}} + \frac{T_{amb}G_{ambcc}}{Q_{in}}\right] + (T_{amb} - T_{sink})\left[1 - exp\left(-\frac{G_L}{Q_{in}}\frac{\Delta h_v}{c_{pl}}\right)\right]}{1 - \frac{1}{Q_{in}}\left[\frac{1}{\rho v c_{pl}}(G_{cv} + G_{axw})(\Delta P_{ll} + \Delta P_{vl} + \Delta P_{vg} + \Delta P_w - \rho_l g \Delta H) - \frac{\Delta h_v}{c_{pl}}G_{ambcc}\right]} \tag{34}$$

$$T_{cc_{FCM}} = T_{sink} + \frac{Q_{in}}{G_c}\frac{1 + \frac{G_{axw}}{G_{ev}}\frac{G_c}{G_{sub}}\frac{A_{sub}}{A_c}}{1 + \frac{G_{axw}}{G_{ev}}} \tag{35}$$

The entire profile of T_{cc} is deduced from the following equation

$$T_{cc} = max(T_{ccVCM}, T_{ccFCM}) \tag{36}$$

5. Detailed Analysis of The Heat Transfer in The Evaporator Section

The heat transfer analysis of the LHP operation which is detailed in the previous section demonstrates the need for knowledge of the heat transfer coefficient of evaporation within the porous wick. As it is highlighted in the review study of the models which is presented in section 2, the heat transfer coefficients of evaporation were calculated by expressions that are not valid for LHP

operation or they are determined so that the experimental results fit those issued from the models. In this section, we propose to present a model that is capable of predicting the wall evaporator temperature and calculating the heat transfer coefficient of evaporation by assessing the experimental results based on dimensionless numbers.

The model considers the following assumptions: (1) a steady-state one-dimensional problem through the capillary structure, (2) the properties of the capillary structure are homogeneous, (3) the saturation temperature is constant throughout the capillary structure, and (4) the porous wick is considered completely saturated. To model the heat transfer within the primary wick, the energy balance can be represented by the heat diffusion equation with a source term according to Gabsi *et al.,* [52]

$$\frac{d^2T}{dx^2} - \frac{p_{ev}}{\lambda_{peff}} = 0 \tag{37}$$

λ_{peff} is the effective thermal conductivity of the porous structure. p_{ev} is the heat source term per unit of volume due to evaporation within the porous structure. It can be written as

$$p_{ev} = a \, A_p [T(x) - T_v]^b \tag{38}$$

a and b are constants that can be determined experimentally. A_p is the specific area per unit of the porous wick volume which is given by

$$A_p = 3 \, (1 - \varphi_w)/R_p \tag{39}$$

where R_p is the pore radius. The combination of Eq. (37) and Eq. (38) yields

$$\frac{d^2T}{dx^2} - \frac{a \, A_p [T(x) - T_v]^b}{\lambda_{peff}} = 0 \tag{40}$$

As the porous structure is considered thick and the specific area is large, the heat transfer throughout the capillary structure can be considered through a wall of semi-infinite thickness, and the expression of the temperature distribution within the wick is as follows

$$\theta(x) = [\left(\frac{b-1}{2}\right)\sqrt{\frac{2aA_p}{\lambda_{peff}(b+1)}}x + \theta_{ev}^{(1-b)/2}]^{2/(1-b)} \tag{41}$$

where $\theta(x) = T(x) - T_v$ and $\theta_{ev} = T_{ev} - T_v$.

The net input heat flux serving for the evaporation, q_{ev}, obtained by excluding the axial thermal conduction and the heat losses to the ambient air, is equal to the heat flux transferred by evaporation within the porous structure q_{evp}, and that transferred by conduction through the porous structure, q_{cd}. This energy balance can be written as:

$$q_{ev} = q_{evp} + q_{cd} = \varphi_p a \theta_w^b - \lambda_{peff} \frac{d\theta}{dx}\Big|_{x=0} \tag{42}$$

The heat flux, q_{ev}, is calculated based on the heat transfer active area, A_{ev}, of the evaporator. By substituting Eq. (41) into Eq. (42), we obtain

$$q_{ev} = \varphi_p a\theta_{ev}{}^b + \sqrt{\frac{2a\,A_p\,\lambda_{peff}}{(b+1)}}\,\theta_{ev}{}^{(1+b)/2} \qquad (43)$$

Knowing q_{ev}, q_{ev} is calculated by iteration method and this needs the complete knowledge of the constants a and b which are determined experimentally. Gabsi *et al.,* [52] developed a correlation based on the Vaschy-Bakingham theorem and led to the definition of dimensionless numbers containing the thermophysical properties of the working fluid and the geometrical parameters of the LHP. This correlation is written as follows

$$Nu = A\,Re^m Kp^n Pr^o Ja^{*p} \qquad (44)$$

A*, m, n, o, and p are coefficients. The Nusselt number, Nu, is defined as follows

$$Nu = \frac{h_{ev}\,D_g}{\lambda_l} = \frac{Q_{ev}\,D_g}{(T_{ev}-T_v)\,A_{ev}\,\lambda_l} \qquad (45)$$

A_{ev} is the heat exchange surface of the evaporator active area. T_{ev} and T_v are the evaporator wall and vapor temperatures, respectively. D_g is the groove height. The Reynolds number is expressed as

$$Re = \frac{\dot{m}\,D_g}{\mu_l\,A_g} = \frac{Q_{ev}\,D_g}{\Delta h_v\,\mu_l\,A_g} \qquad (46)$$

The Prandtl number is given by

$$P_r = \frac{\mu_l c_{pl}}{\lambda_l} \qquad (47)$$

The dimensionless number, K_p, is the Kutateladze number calculated according to:

$$K_p = \frac{P_{sat}\,La}{\sigma} \qquad (48)$$

La is the Laplace number defined as

$$La = \sqrt{\sigma/g(\rho_l - \rho_v)} \qquad (49)$$

The modified Jackob number is expressed as

$$J_a^* = \frac{\rho_l\,c_{pl}T_{sat}}{\rho_v\,\Delta h_v} \qquad (50)$$

The Nusselt number is calculated using the experimental values of T_{ev} and T_v as a function of the heat input power. The other dimensionless numbers are calculated by considering the thermophysical properties of the working fluid at the film temperature

$$T_{film} = \frac{T_{ev}+T_v}{2} \qquad (51)$$

The experimental value of the thermal resistance of the evaporator, R_{ev}, is calculated as follows

$$R_{ev} = \frac{T_{ev} - T_v}{Q_{ev}} \tag{52}$$

The evaporation heat transfer coefficient, h_{ev}, is then deduced from

$$h_{ev} = \frac{1}{R_{ev} A_{ev}} \tag{53}$$

Taking into account the different expressions of the dimensionless numbers and relation in Eq. (44), the expression of Q_{ev} can be determined according to

$$Q_{ev} = [(\lambda_l A_{ev}/D_g) \times A(D_g/\mu_l \Delta h_v A_{ev})^m \times Ja^{*n} \times K_p{}^p]^{(1/1-m)} (T_{ev} - T_v)^{(1/1-m)} \tag{54}$$

Given that $Q_{ev} = p_{ev}/A_p$ and compared with the Eq. (38), we deduce

$$a = [(\lambda_l A_{ev}/D_g) \times A \times (D_g/\mu_l \Delta h_v A_g)^m \times (\rho_l C_{pl} T_{sat}/\rho_v \Delta h_v)^n (P_{sat} La/\sigma)^p]^{(1/1-m)} \tag{55}$$

$$b = 1/(1 - m) \tag{56}$$

The thermal conductance, G_{sp}, is calculated according to

$$G_{sp} = Q_{ev}/\theta_{ev} \tag{57}$$

The coefficients of Eq. (44) are determined by a multiple linear regression for each heat sink temperature, T_{sink}. The obtained values are listed in Table 6. The coefficients m and o are set to 2/3 and 0 respectively to refine the results. Figure 4 represents the variations of the Nusselt number, Nu_{cal}, calculated from Eq. (44) as a function of that determined experimentally, Nu_{exp}, based on the experimental values of the evaporation heat transfer coefficient, h_{ev}. It is noted that there is a good agreement between the experimental results and those obtained by the correlation for each T_{sink}. Indeed, the relative discrepancy between Nu_{exp} and Nu_{cal} varies between ± 10 % for $T_{sink} = 80°C$ and ± 25 % for $T_{sink} = 20°C$. This correlation would allow refining the results of the model. Indeed, from this correlation, the thermal conductance of the evaporator, G_{ev}, can be determined to compute the temperature of the evaporator, T_{ev}, and that of the vapor, T_v.

Table 6
Coefficients of Eq. (44) for each sink temperature

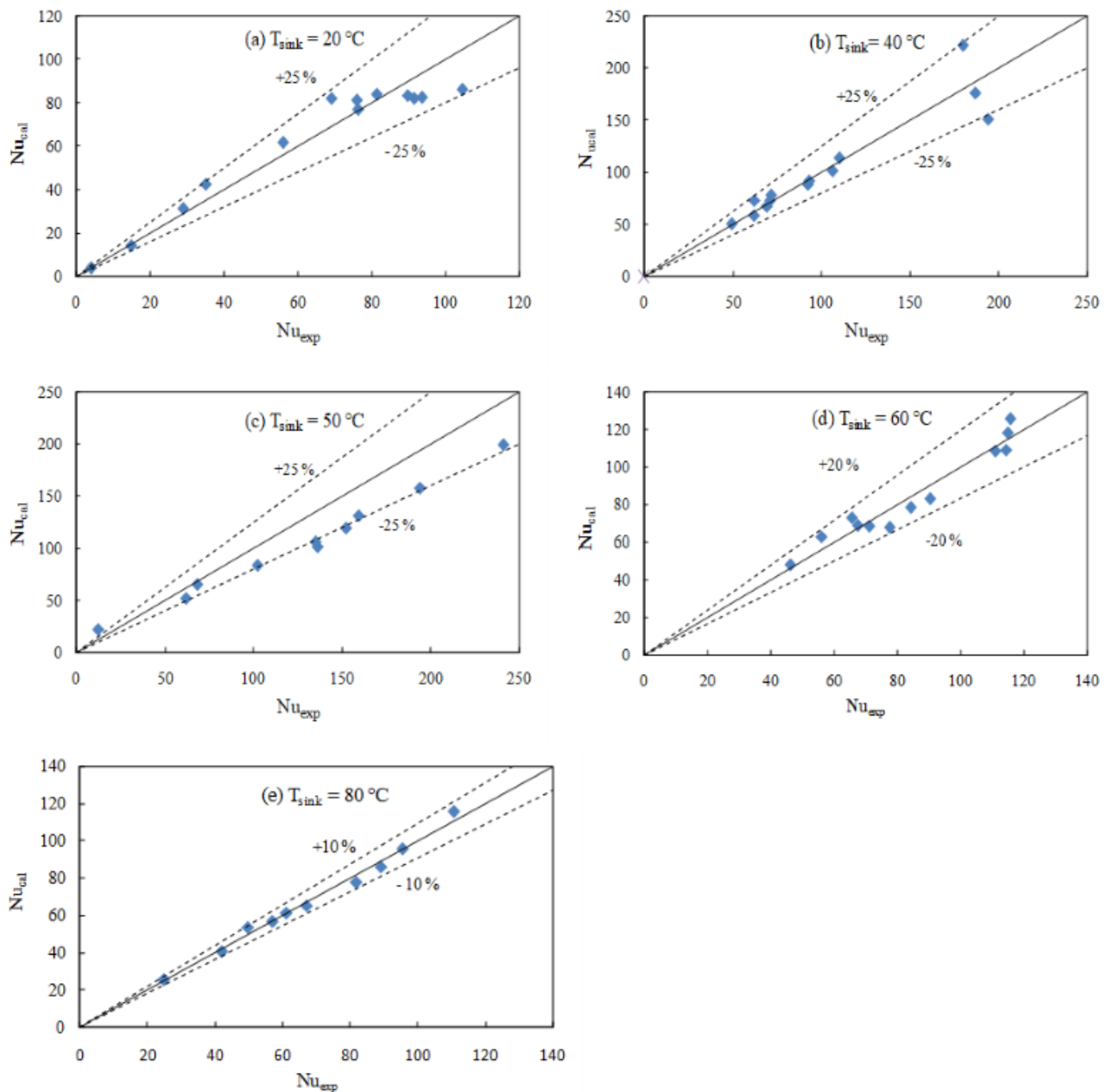| T_{sink} (°C)	m	n	o	p	Ln(A)	Relative discrepancy according to the experiments
20	2/3	4.757	0	3.050	-44.173	± 25 %
40	2/3	4.160	0	2.916	-39.337	± 25 %
50	2/3	8.224	0	5.105	-77.540	± 25 %
60	2/3	6.469	0	4.605	-63.086	± 20 %
80	2/3	4.290	0	3.707	-43.467	± 10 %

Fig. 4. Variations of Nu_{cal} versus Nu_{exp} for different heat sink temperatures: (a) T_{sink} = 20°C, (b) T_{sink} = 40°C, (c) T_{sink} = 50°C, (d) T_{sink} = 60°C, (e) T_{sink} = 60°C, and (f) T_{sink} = 80°C

6. Model Validation

6.1 Validation for The Evaporator and Vapor Temperatures

The variations of the evaporator and vapor temperatures obtained experimentally by Chernysheva *et al.,* [26] are shown in Figure 5 for different heat sink temperatures, T_{sink} = 20, 40, and 50°C. For these tests, the LHP is positioned horizontally. Table 7 shows the different values of h_{sink} for each sink temperature calculated based on the indicated volume flow rate in the study of Maydanik *et al.,* [27] using the Dittus-Boelter correlation [59]. The convective heat transfer coefficient between the LHP and the ambient is h_{amb} = 10 W/m.K and the ambient temperature T_{amb} = 20°C.

Table 7
Values of h_{sink} for each heat sink temperature

| T_{sink} (°C)	20	40	50	60	80
h_{sink}(W/m².K)	9000	11893	13029	13981	15729

For T_{sink} = 20°C, the LHP operates in VCM mode for heat loads lower than 150 W and FCM mode for heat input higher than 150 W. It is noticed that the experimental values of the temperatures T_{ev} and T_v are higher than those obtained from the model (Figure 5(a) and Figure 5(b)). Hence, the model underestimates the experimental results for both modes. The discrepancy between the experimental results and those of the model can be explained experimentally by the generation of non-condensable gases in the compensation chamber and the condenser. Indeed, it is well known that the effect of non-condensable gases is effective for low heat sink temperatures, since, in these conditions, their volume is high, which alters the condensation phenomenon and the heat transfer in the compensation chamber. It is also noted that the gap between the experimental values and those resulting from the model increases for high input powers. This can be explained by the fact that these heat loads exceed the capillary limit Q_{max}. Consequently, the porous capillary structure becomes starved of liquid, and dry-out happens. As a result, the temperatures (T_{ev} and T_v) increase excessively. As the model does not take into account the LHP operation in these particular conditions (presence of non-condensable gas and dry-out), the theoretical calculations do not retrieve the experimental values quantitatively but qualitatively since the model can predict the U-shape curve corresponding to the variations of the compensation chamber temperature with the heat load. Here, we can note that Chernysheva *et al.,* [53] computed the theoretical calculations to retrieve the experimental variations of the vapor temperature as a function of the heat load for T_{sink} = 20°C for two LHPs: LHP#1 and LHP#2 (LHP#1 is the same LHP considered in this study). The comparison between the experimental and computed results indicated that the calculated values underestimate the experimental ones in the VCM, as is found in this study.

For T_{sink} = 40°C, the LHP operates in the VCM mode for heat input power less than 100 W and the FCM mode for heat input powers ranging between 100 and 400 W (Figure 5(c) and Figure 5(d)). Here, the gap between the experimental values and the computed ones is reduced in both operating modes. However, for heat input powers higher than 400 W, there is a rapid increase in T_{ev} and T_v leading to an increase in the gap between the computed temperatures by the model and those resulting from the experimental tests. Indeed, for these heat input powers, the capillary limit is exceeded, leading to the dry-out phenomenon. Here, again we can note that the comparison between the experimental vapor temperatures and the computed ones by Chernysheva *et al.,* [53] shows a gap for the two operating modes. Indeed, the computed values underestimate the experimental ones.

For T_{sink} = 50°C, the LHP operates in VCM mode for heat input powers less than 50 W and FCM mode for heat input powers ranging between 50 W and 450 W (Figure 5(e) and Figure 5(f)). We also note that by increasing T_{sink}, the heat input power range corresponding to the VCM mode decreases. The comparison between the calculated and the measured values of T_{ev} and T_v shows that there is a good agreement for a wide range of the heat input powers, except for heat loads above 450 W, for which the discrepancy between the calculated and measured temperatures increases. For these heat input powers, the capillary limit is exceeded, and the dry-out occurs in the evaporator.

For T_{sink} = 60°C, the LHP works only in FCM operating mode. Hence, a linear increase in the temperatures T_{ev} and T_v is obtained (Figure 5(g) and Figure 5(h)). There is good agreement between the model and the experiment for heat input powers below 550 W. Beyond this power, a gap between the calculated and the measured temperatures are observed, which shows that the capillary limit is reached and even exceeded.

For T_{sink} = 80°C, the temperature variations are linear, indicating that the LHP operates in FCM mode over the full heat input power range (Figure 5(i) and Figure 5(j)). We note that there is a very satisfactory agreement between the model and the experiment for all the heat input powers. It should be noted that for this test, the capillary limit is not reached. Indeed, Chernysheva *et al.,* [26] stopped the test at a power of 450 W before reaching the capillary limit, thus avoiding a high overpressure in the LHP since, under these conditions, the temperature of the vapor exceeds 100°C.
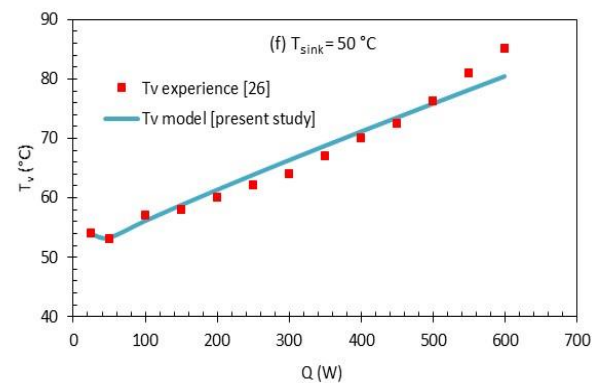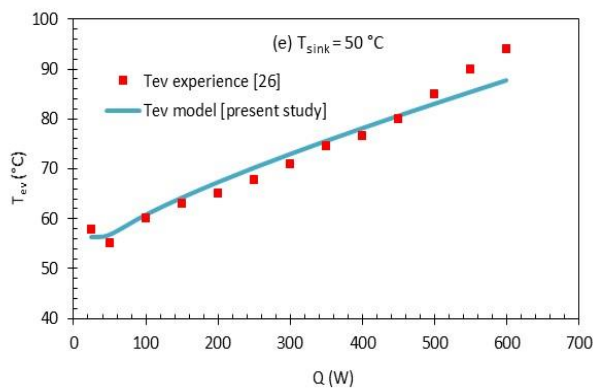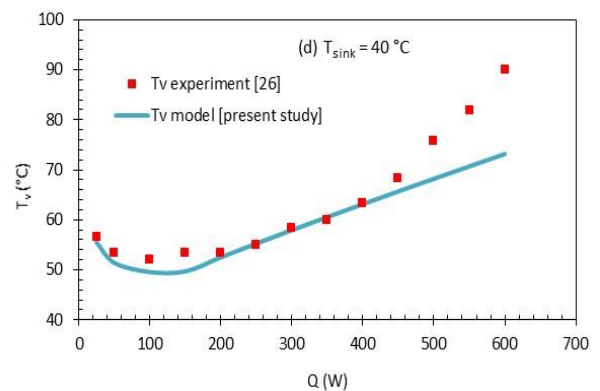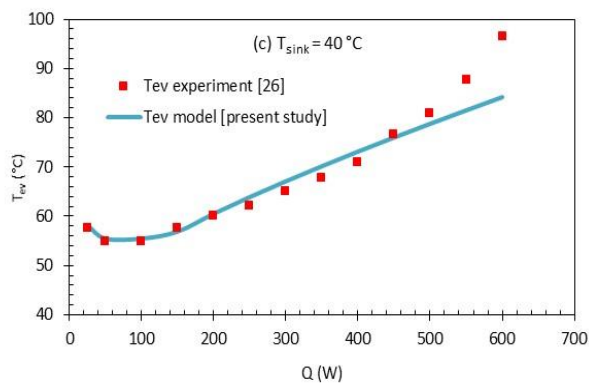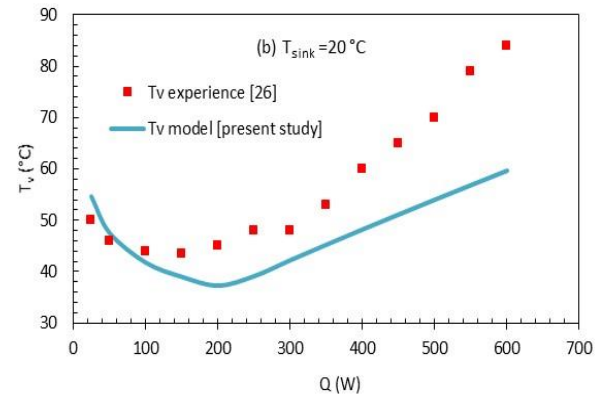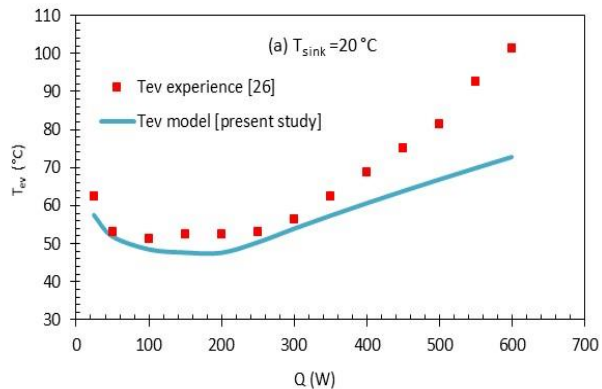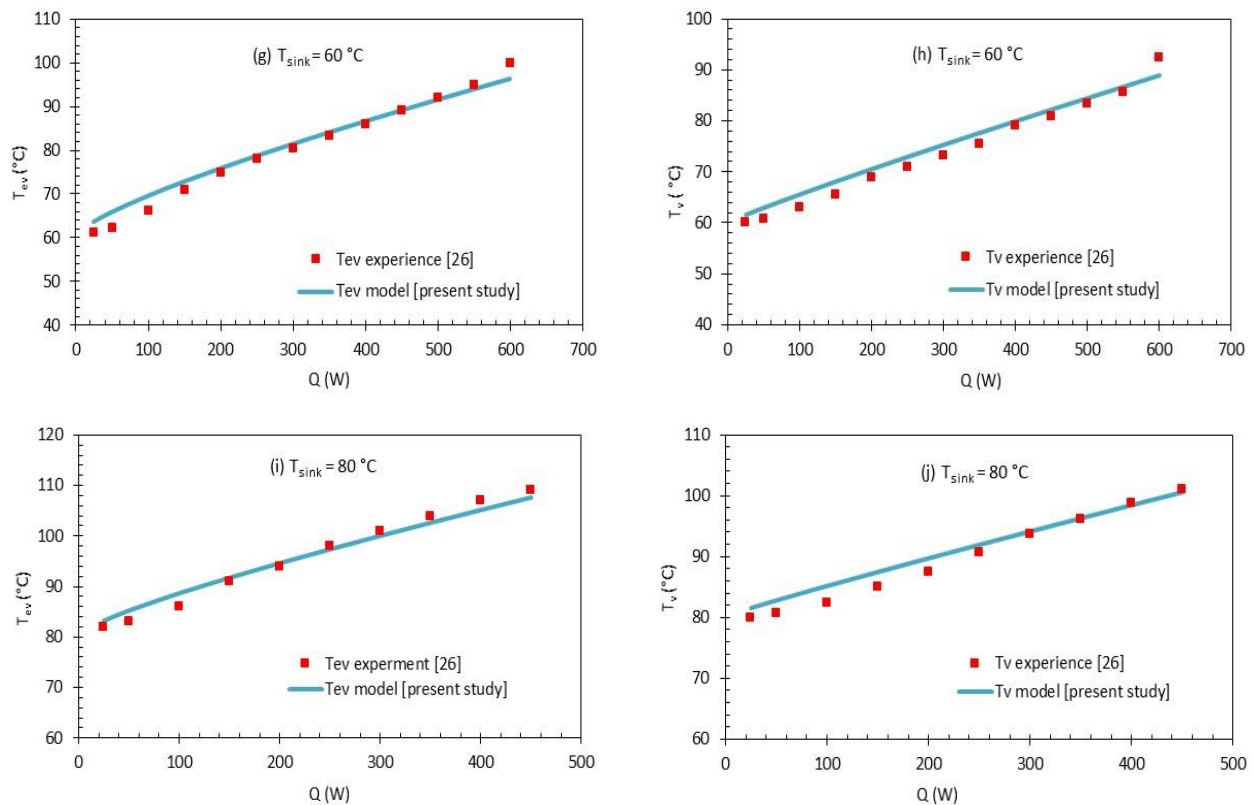
Fig. 5. Variations of the evaporator and vapor temperatures as a function of the heat load for various sink temperatures: (a)-(b) T$_{sink}$ = 20°C, (c)-(d) T$_{sink}$ = 40°C, (e)-(f) T$_{sink}$ = 5 °C, (g)-(h) T$_{sink}$ = 60°C, and (i)-(j) T$_{sink}$ = 80°C

Table 8 lists the values of the coefficient of correlation, R^2, which compares the experimental values of the evaporator and vapor temperatures to those computed by the model for different heat sink temperatures [26]. For the evaporator temperature, R^2 ranges between 0.953 and 0.998; however, for the vapor temperature, it varies between 0.953 and 0.997 for T$_{sink}$ ranging between 40 and 80°C. The lowest R^2 is for T$_{sink}$ = 20°C for the reasons indicated above.

Table 8
Values of R^2 for T$_{ev}$ and T$_v$ for each heat sink temperature

T$_{sink}$ (°C)	20	40	50	60	80
R^2 for T$_{ev}$	0.974	0.970	0.953	0.998	0.998
R^2 for T$_v$	0.850	0.954	0985	0.993	0.997

6.2 Validation for The Capillary Limit

The expression of the capillary limit is given by Eq. (1). The capillary limit is calculated for different inclinations and is compared to the values computed by Chernysheva *et al.,* [26]. It increases almost linearly as a function of the vapor temperature for different tilt angles. It can be noted that there is good agreement between the results of the proposed model and those computed by Chernysheva *et al.,* [26] (Figure 6). Table 9 lists the values of the coefficient of correlation, R^2, which compares the values computed by the model of Chernysheva *et al.,* [26] to those computed by the present model, for different inclinations. R^2 varies between 0.994 and 0.998 for the considered tilt angle range.

Table 9
Values of R^2 for Q_{max} for each inclination

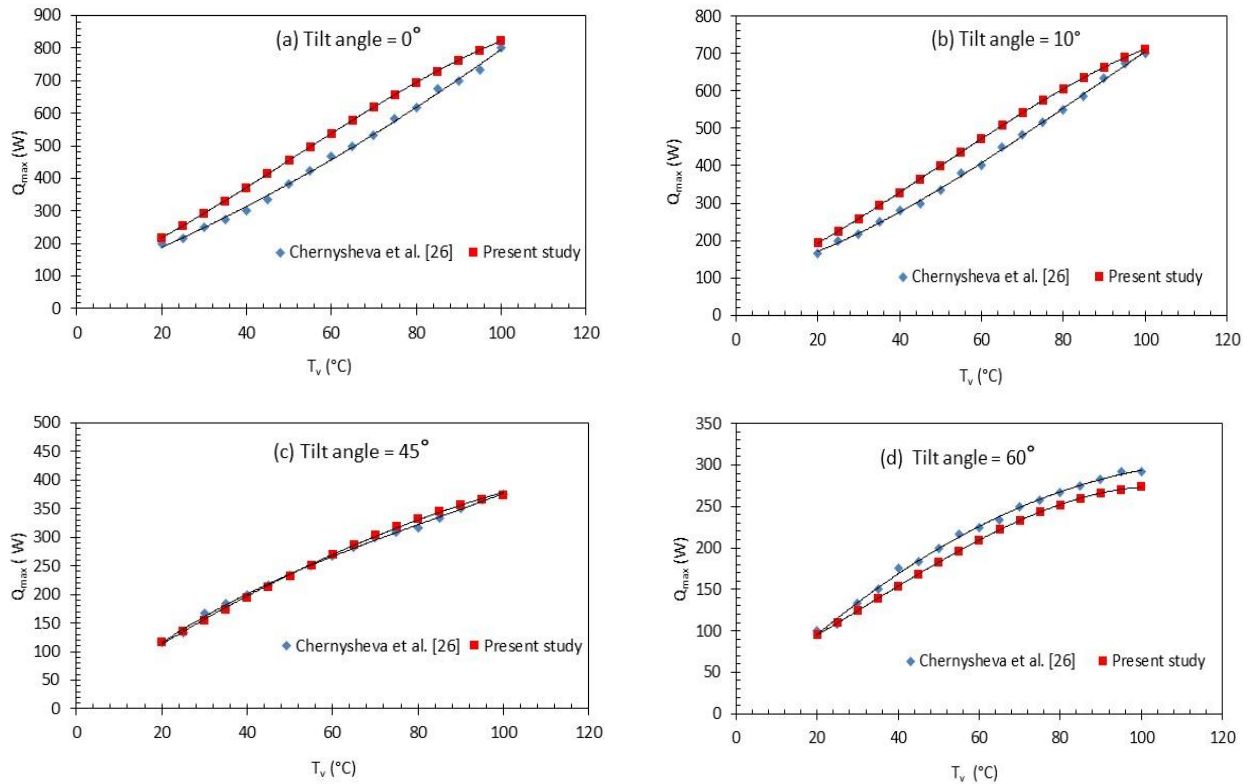| Inclination	0°	10°	45°	60°
R^2 for Q_{max}	0.995	0.994	0.997	0.998

Fig. 6. Comparison between the capillary limit calculated from the proposed model and that of Chernysheva *et al.,* [26] for different tilts: (a) 0°, (b) 10°, (c) 45°, and (d) 60°

6.3 Validation for The Evaporator Thermal Resistance

The experimental evaporator thermal resistance, R_{evexp}, is deduced from the values of the evaporator wall and the vapor temperatures measured for each cooling temperature, T_{sink} according to Eq. (52). The thermal resistance of the evaporator calculated by the model, R_{evm}, is deduced from Eq. (21). A comparison between the results of the experiments and those resulting from the model for different sink temperatures is shown in Figure 7. The curve showing the evolution of the evaporator thermal resistance as a function of the heat input power generally decreases in the VCM mode, which is characterized by the simultaneous decrease of T_{ev} and T_v. Beyond the transition power, the thermal resistance of the evaporator becomes almost constant in the FCM mode. For T_{sink} = 20°C, we notice that there is a large gap between R_{evexp} and R_{evm}, especially in the VCM operating mode. However, the gap between the experimental values and those computed from the proposed model for both operating modes becomes smaller for the other cooling temperatures. Generally, the computed values are closer to those obtained from the experiments, which proves the reliability of the proposed model for the evaporation phenomenon.

Table 10 lists the values of the coefficient of correlation, R^2, which compares the experimental values of Chernysheva *et al.,* [26] to those computed by the present model for different sink temperatures. The values of R^2 are lower than those obtained for T_{ev} and T_v. This can be explained by the experimental uncertainties in calculating R_{ev}. Indeed, the highest gap between the experimental

values of R_{ev} and the computed ones is obtained in the VCM operating mode, for which the heat loads and the difference ($T_{ev}-T_v$) are low. Hence, the experimental uncertainties for this operating mode are high, especially for low heat sink temperatures.

Table 10
Values of R^2 for R_{ev} for each heat sink temperature

Inclination	20°C	40°C	50°C	60°C	80°C
R^2 for R_{ev}	0.840	0.855	0.876	0.810	0.971
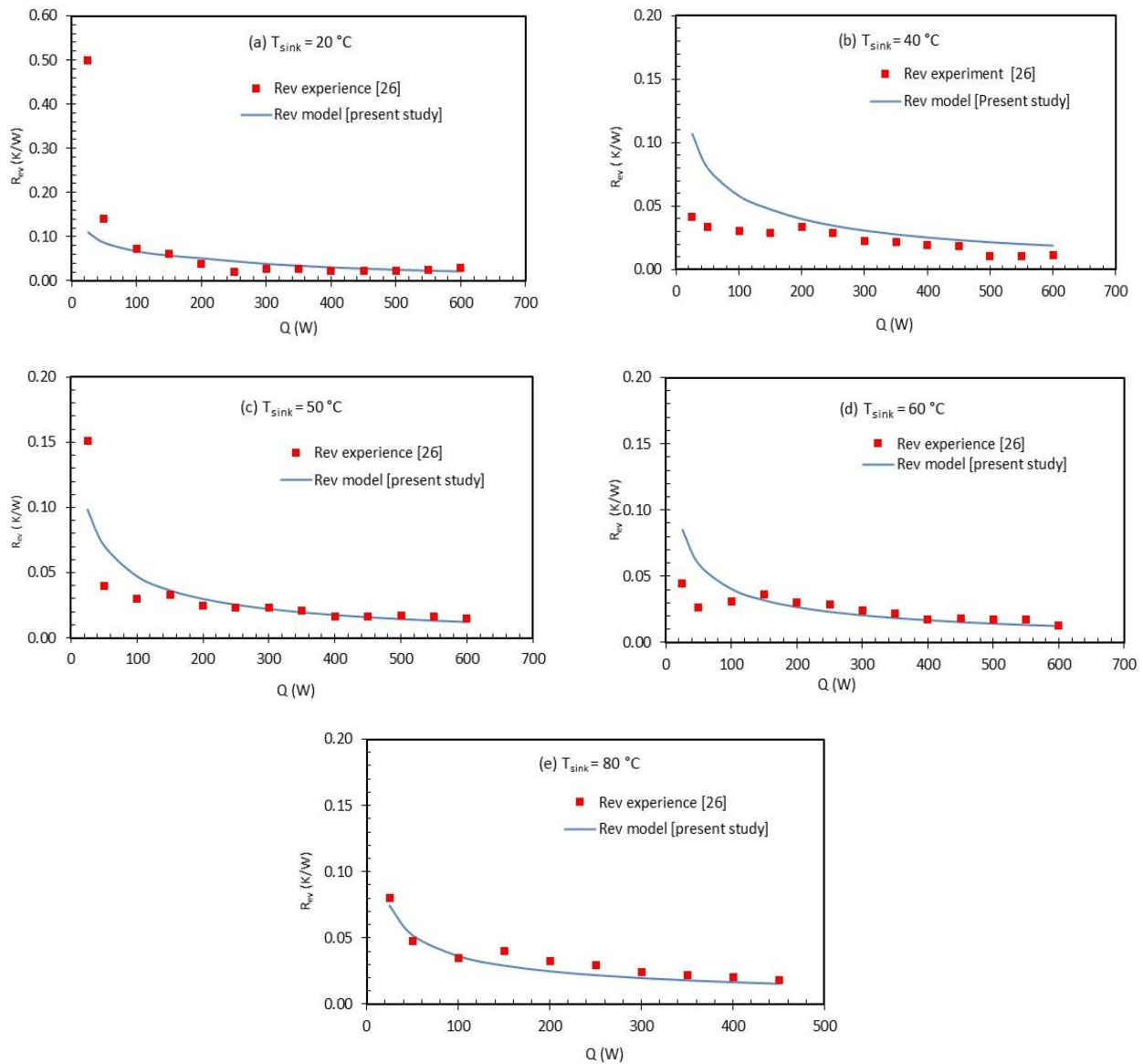
Fig. 7. Evaporator thermal resistances for different sink temperatures: (a) T_{sink} = 20°C, (b) T_{sink} = 40°C, (c) T_{sink} = 50°C, (d) T_{sink} = 60°C, (e) T_{sink} = 80°C

7. Parametric Study

Several parameters can affect the thermal performance of the LHP, such as the orientation, the sink temperature, the ambient temperature, the heat exchange between the LHP and the ambient, the characteristics of the capillary structure (porosity and material), the dimensions of the grooves, the nature of the fluid, and how the heat is supplied to the evaporator. In what follows, we propose to study the effect of some parameters especially those related to the evaporator, such as the axial thermal conductance, G_{axw}, which affects the heat leaks transferred by conduction between the evaporator and the compensation chamber. Furthermore, since the capillary structure plays an essential role in the LHP operation, we have proceeded to a parametric study, including the wick porosity and material, as well as the groove dimensions (width and depth). In this study, the ambient and sink temperatures are equal to respectively 20°C and 40°C. The ambient and sink heat transfer coefficients are set as respectively 10 and 12,000 W/m².K. The radius pore is equal to 27 μm, and the groove number is 12.

7.1 Effect of The Axial Thermal Conductance Between the Evaporator and The Compensation Chamber

The variations of the evaporator and vapor temperatures as a function of the heat input power for different values of G_{axw} and $T_{sink} = 40°C$ are shown in Figure 8. In these simulations, the porosity and the depth and width of the groove are equal to 0.46, 1.8, and 1.8 mm, respectively. The capillary structure material is copper.

When the LHP operates in VCM mode, the heat flux rate serving to the evaporation decreases if the heat leaks transferred by thermal conduction between the evaporator and the compensation chamber walls increase (i.e., G_{axw} increases). Thus, the amount of vapor formed in the evaporator is reduced. Hence, the condensate, which leaves the condenser, is less sub-cooled when the axial heat leaks between the evaporator and the compensation chamber increase. As a result, the evaporator and vapor temperatures increase (Figure 8(a) and Figure 8(b)).

In the FCM operating mode, the mass of the vapor formed in the evaporator increases; However, the increase of the axial wall heat leaks between the evaporator and the compensation chamber reduces the vapor formation. Thus, the excess of the vapor produced by the increase of the imposed power is compensated by a mass defect of the vapor induced by the axial wall heat leaks. Consequently, the combined effect of both the heat load increase and the axial wall heat leaks hardly affects the amount of the condensate formed in the condenser, and the length of the sub-cooling zone is not so affected. Thus, the temperatures of the condensate at the outlet of the condenser and the inlet of the compensation chamber are hardly affected by this combined effect since the pressure losses in the liquid line are not affected so much. Therefore, the temperature of the evaporator and that of the vapor are barely affected by the axial wall heat leaks. The capillary limit, which constitutes the maximum heat input beyond which dry-out starts, increases with the axial thermal conductance between the evaporator and the compensation chamber, G_{axw}. Indeed, the rise of the vapor temperature level in the LHP due to the G_{axw} increase causes a reduction of the vapor pressure drop in the grooves ΔP_{vg} since the vapor dynamic viscosity decreases. Hence, the driving capillary pressure, ΔP_{cap}, can overcome the pressure drops easily, and consequently, the capillary limit increases. The capillary limits for G_{axw}= 0.45, 0.56, and 0.67 W/K are 480, 485, and 490 W, respectively. The heat input powers which are considered in the simulations are limited to the capillary limits since the model does not take into account the dry-out phenomenon in the mathematical formulation.
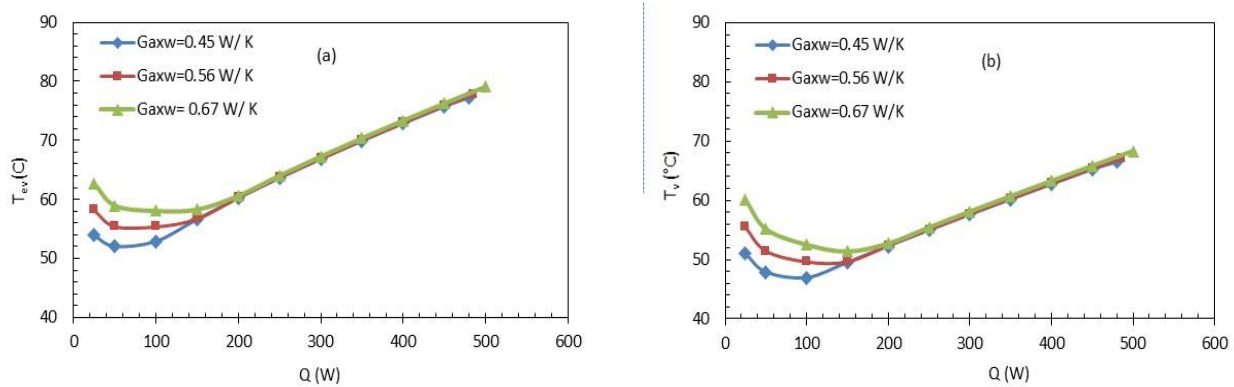
Fig. 8. Temperature variations for different values of G_{axw}: (a) evaporator temperature, (b) vapor temperature

7.2 Effect of The Capillary Structure Porosity

The variations of the evaporator and vapor temperatures as a function of the heat input power, for different porosities (T_{sink}= 40°C) are shown in Figure 9. In these simulations, the groove depth and width are both equal to 1.8 mm and the conductance G_{axw} is equal respectively to 0.67 W/K. The material used for the capillary structure is copper.
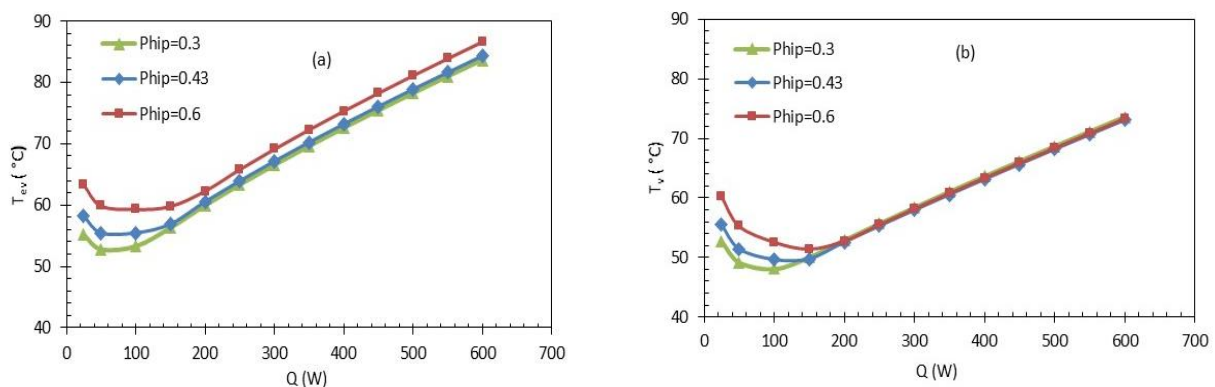

Fig. 9. Temperature variations for different porosities: (a) evaporator temperature, (b) vapor temperature

In the VCM operating mode, the evaporator and vapor temperatures increase with porosity; however, for the FCM operating mode, the evaporator and vapor temperatures are hardly affected by porosity. In the VCM operating mode, as the porosity increases, the effective thermal conductivity of the porous structure decreases, which leads to an increase in the evaporator thermal resistance. Thus, for an imposed heat input power, the evaporator temperature increases with porosity (Figure 9(a)). Besides, when porosity increases for an imposed heat input power, the amount of liquid coming from the compensation chamber augments due to the permeability of the capillary structure increase with porosity. Thus, the evaporation is intensified, causing an increase in the mass of the vapor and its temperature (Figure 9(b)). In the FCM operating mode, the imposed powers being much higher than those of the VCM operating mode, the vapor mass-produced in the evaporator is high. Thus, for a given power, the increase in the vapor mass with the porosity is not significant compared to that induced by the heat load increase, and consequently, the evaporator and vapor temperatures are not affected so much by the porosity increase. It is worth noting that augmenting the porosity causes a reduction in the vapor pressure drop in the grooves. Consequently, the capillary driving pressure

can overcome the pressure drops easily, and the capillary limit is increased. Hence, the capillary limits for φ_p= 0.3, 0.4, and 0.46 are 100, 330, and 485W, respectively.

7.3 Effect of The Capillary Structure Material

The variations of the evaporator and the vapor temperatures as a function of the heat load for different capillary structure materials: copper (λ_{copper} = 390 W/m.K) and nickel (λ_{nickel} = 90 W/m.K) are depicted in Figure 10. The porosity and the conductance G_{axw} are equal to respectively 0.46 and 0.67 W/m². Both the groove depth and width are equal to 1.8 mm.

The nature of the material affects the evaporator temperature for both operation modes (Figure 10(b)). The use of a capillary structure made in nickel leads to high evaporator temperatures compared to those obtained with copper. The vapor temperature is sensitive to the capillary structure material in the VCM mode. However, it is not substantially affected by this parameter in FCM operating mode. The transition power increases with the decrease of the capillary structure's thermal conductivity. Indeed, for nickel and copper, the transition power is 200 and 100 W, respectively.
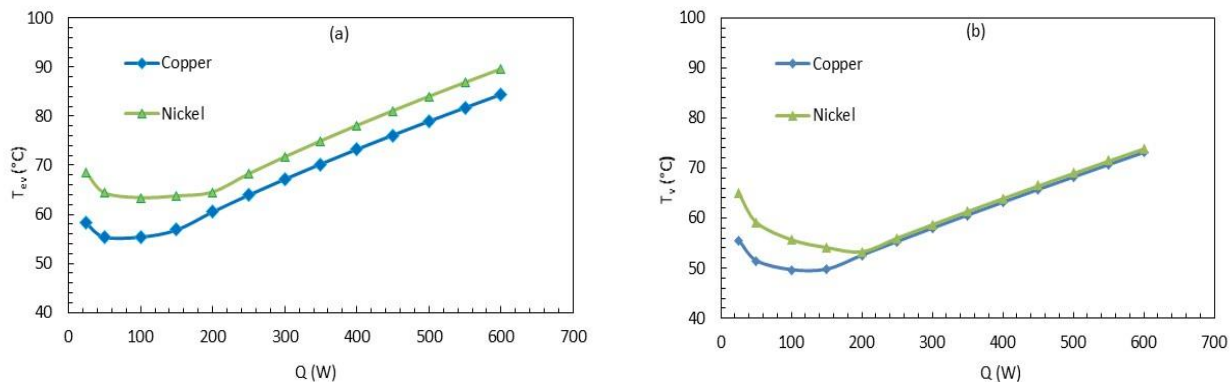

Fig. 10. Temperature variations for different capillary structure materials: (a) evaporator temperature, (b) vapor temperature

The evaporator temperature increase is due to that of the evaporator thermal resistance caused by the decrease of the capillary structure thermal conductivity (Figure 10(a)). Likewise, the use of a low conducting material augments the axial heat leaks transferred by conduction between the evaporator wall and the compensation chamber wall, thus reducing the heat flux rates necessary for the evaporation of the liquid in the capillary structure. The decrease of the temperature in the LHP due to the increase of the capillary structure thermal conductivity reduces the pressure drops since the dynamic viscosity decreases with temperature. Hence, the driving capillary pressure overcomes the pressure drops easily. Consequently, the capillary limit is increased. The capillary limits for copper and nickel are 485 and 525 W, respectively.

7.4 Effect of The Groove Dimensions

The variations of the evaporator and vapor temperatures as a function of the imposed power for different groove depths, D_g, are shown in Figure 11. For these simulations, W_g is equal to 1.8 mm. The values of the porosity and G_{axw} are respectively 0.46 and 0.67 W/K. Copper is the capillary structure material.

In VCM mode, these temperatures increase with the groove depth; nevertheless, in FCM mode, the groove depth hardly affects the evaporator and the vapor temperatures. In VCM mode, and for a given heat load, the evaporator temperature increase with the groove depth is mainly due to the augmentation of the conductive thermal resistance, which can reduce the heat flux rate necessary for the evaporation within the capillary structure. This also increases the vapor temperature. In FCM mode, the depth of the grooves does not affect the temperature levels since the heat transfer in this operation mode is controlled by the heat sink. It can also be noticed that the transition power increases slightly with the groove depth. The amount of vapor formed in the grooves due to the evaporation is reduced when the depth of the grooves increases. Consequently, the vapor pressure drops in the grooves decrease. Hence, the driving capillary pressure can overcome all the pressure drops easily, causing an increase in the capillary limit. The capillary limits for D_g= 1, 1.8, and 2.5 mm are 240, 485, and 750 W, respectively.
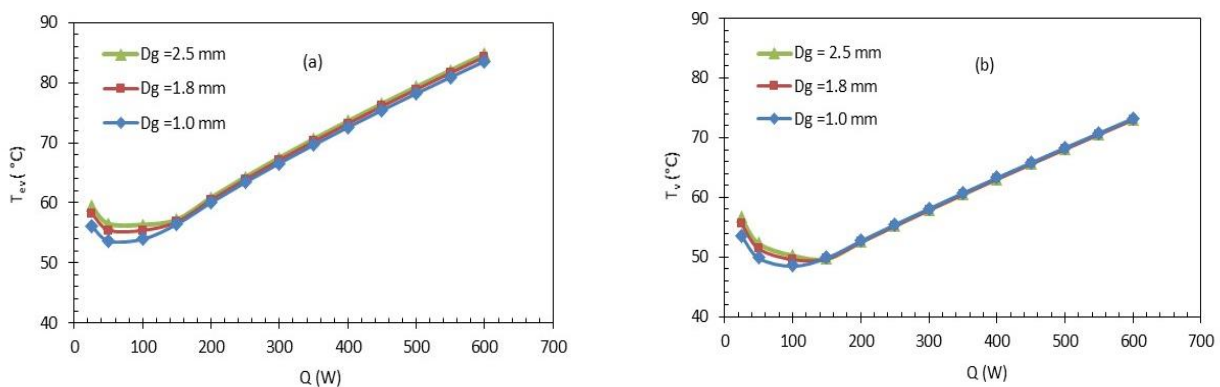

Fig. 11. Effect of the groove depth on (a) the evaporator temperature and (b) the vapor temperature

The effect of the groove width, W_g, on the evaporator, and vapor temperatures are shown in Figure 12. In these simulations, D_g is fixed to 1.8 mm. The increase of the groove width causes a slight decrease in these temperatures. Indeed, to preserve the number of grooves, as the width of the groove increases, the groove spacing decreases. Thus, there is less material, and the conductive heat transfer decreases in favor of the heat transfer by phase change. The reduction of the temperature level due to the decrease of the groove width is obvious in the VCM. Indeed, the amount of vapor formed in the VCM is usually not important, and with the reduction of the heat flux responsible for the evaporation of the liquid, the effect of the W_g becomes more noticeable. Consequently, the power transition increases when the groove width increases.
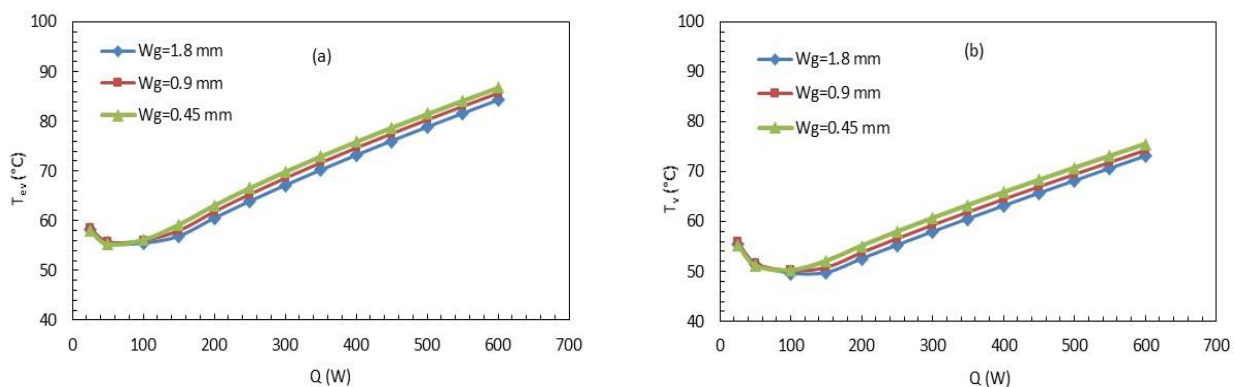

Fig. 12. Effect of the groove width on (a) the evaporator temperature and (b) the vapor temperature

The effect of the groove width on the capillary limit is the same as that of the groove depth. Indeed, the increase of W_g induces the reduction of the groove spacing S_g. Accordingly, the heat exchange area is reduced. This influences the heat flux rate responsible for the evaporation of the liquid within the sintered powder, which is reduced. The amount of vapor formed in the grooves is not important for large groove width, and consequently, the vapor pressure drop in the grooves is reduced. Since the other pressure drops in the LHP are not affected by W_g, the capillary pressure can overcome these pressure drops easily. The capillary limits for W_g = 0.45, 0.9, and 1.8 mm are 90, 250, and 485 W, respectively.

8. Conclusion

In this paper, an analytical model of an LHP has been developed in steady-state operation. It is based on mass, momentum, and energy balance equations, as well as the thermodynamic relationships. The model allows calculating the temperature of the LHP components and the pressure losses for different operating conditions and different geometrical characteristics of the LHP. The heat transfer device used for the simulations is a copper-water LHP with a flat-evaporator tested by Chernysheva *et al.,* [26] for heat loads ranging from 5 to 600 W at a horizontal position. A satisfactory agreement was found between the computed and experimental results.

A parametric study, including the effects of the axial conductive heat leaks, porosity, the material of the capillary structure, and the groove dimensions, was carried out. The results are summarized in Table 11. The effects of the studied parameters on the LHP thermal performances are different according to the operating modes.

Table 11
Summary of the effect of the studied parameters

Parameter Trend	VCM Mode	FCM Mode
G_{axw} increases	T_{ev} & T_v increase	T_{ev} & T_v not affected
Porosity increases	T_{ev} & T_v increase	T_{ev} increases & T_v not affected
Wick thermal conductivity increases	T_{ev} & T_v decrease	T_{ev} decreases & T_v not affected
D_g increases	T_{ev} & T_v increase	T_{ev} & T_v not affected
W_g increases	T_{ev} & T_v not affected	T_{ev} & T_v decrease

For the VCM operating mode, the increase of the heat leaks by conduction between the evaporator and the compensation chamber, porosity, and the groove depth lead to the augmentation of the evaporator and vapor temperatures; However, increasing the wick thermal conductivity occasions a reduction of these temperatures. It is noteworthy that increasing the groove width hardly affects the evaporator and vapor temperatures.

For the FCM operating mode, the evaporator and vapor temperatures are not affected by the conductive heat leaks between the evaporator and the compensation chamber as well as the groove depth. Furthermore, the vapor temperature is not affected by the porosity and the wick thermal conductivity; however, the evaporator temperature increases with the first parameter and decreases with the second one. Increasing the groove width in the FCM operating mode occasions a decrease in the evaporator and vapor temperatures.

The present work proposes an original method that consists of using dimensional analysis to determine the evaporation heat transfer coefficient from the model and it also proposes original modeling of the phenomenon of evaporation in LHPs. The study aims to model the operation of an LHP in a steady-state regime to determine its thermal performance (capillary limit, thermal resistance, and temperature of the evaporator) for different operating conditions (input power, the

temperature of the cold source, ambient temperature, convection with the ambient, thermal leaks to the compensation chamber, and gravity) as a function of the geometric parameters (diameters and lengths of the liquid and vapor lines, condensation surface, and width and depth of the grooves) and the properties of the capillary structure (porosity, material, and permeability).

References

[1] Hodot, Romain, Valérie Sartre, Frédéric Lefèvre, and Claude Sarno. "Modeling and experimental tests of a loop heat pipe for aerospace applications." *Journal of Thermophysics and Heat Transfer* 30, no. 1 (2016): 182-191. https://doi.org/10.2514/1.T4551

[2] Sarno, C., C. Tantolin, R. Hodot, Yu Maydanik, and S. Vershinin. "Loop thermosyphon thermal management of the avionics of an in-flight entertainment system." *Applied Thermal Engineering* 51, no. 1-2 (2013): 764-769. https://doi.org/10.1016/j.applthermaleng.2012.10.012

[3] Singh, Randeep, Aliakbar Akbarzadeh, Chris Dixon, Mastaka Mochizuki, and Roger R. Riehl. "Miniature loop heat pipe with flat evaporator for cooling computer CPU." *IEEE Transactions on Components and Packaging Technologies* 30, no. 1 (2007): 42-49. https://doi.org/10.1109/TCAPT.2007.892066

[4] Singh, Randeep, Aliakbar Akbarzadeh, and Masataka Mochizuki. "Operational characteristics of a miniature loop heat pipe with flat evaporator." *International Journal of Thermal Sciences* 47, no. 11 (2008): 1504-1515. https://doi.org/10.1016/j.ijthermalsci.2007.12.013

[5] Singh, Randeep, Aliakbar Akbarzadeh, and Masataka Mochizuki. "Effect of wick characteristics on the thermal performance of the miniature loop heat pipe." *Journal of Heat Transfer* 131, no. 8 (2009). https://doi.org/10.1115/1.3109994

[6] Singh, Randeep, Aliakbar Akbarzadeh, and Masataka Mochizuki. "Operational characteristics of the miniature loop heat pipe with non-condensable gases." *International Journal of Heat and Mass Transfer* 53, no. 17-18 (2010): 3471-3482. https://doi.org/10.1016/j.ijheatmasstransfer.2010.04.008

[7] Celata, Gian Piero, Maurizio Cumo, and Massimo Furrer. "Experimental tests of a stainless steel loop heat pipe with flat evaporator." *Experimental Thermal and Fluid Science* 34, no. 7 (2010): 866-878. https://doi.org/10.1016/j.expthermflusci.2010.02.001

[8] Li, Ji, Daming Wang, and G. P. Peterson. "Experimental studies on a high performance compact loop heat pipe with a square flat evaporator." *Applied Thermal Engineering* 30, no. 6-7 (2010): 741-752.

[9] Adoni, Abhijit Avinash, Amrit Ambirajan, V. S. Jasvanth, Dinesh Kumar, and Pradip Dutta. "Theoretical and experimental studies on an ammonia-based loop heat pipe with a flat evaporator." *IEEE Transactions on Components and Packaging Technologies* 33, no. 2 (2010): 478-487. https://doi.org/10.1109/TCAPT.2010.2042056

[10] Liu, Zhichun, Dongxing Gai, Huan Li, Wei Liu, Jinguo Yang, and Mengmeng Liu. "Investigation of impact of different working fluids on the operational characteristics of miniature LHP with flat evaporator." *Applied Thermal Engineering* 31, no. 16 (2011): 3387-3392. https://doi.org/10.1016/j.applthermaleng.2011.06.023

[11] Nguyen, Xuan Hung, Byung Ho Sung, Jeehoon Choi, Seong Ryoul Ryoo, Han Seo Ko, and Chulju Kim. "Study on heat transfer performance for loop heat pipe with circular flat evaporator." *International Journal of Heat and Mass Transfer* 55, no. 4 (2012): 1304-1315. https://doi.org/10.1016/j.ijheatmasstransfer.2011.09.010

[12] Joung, Wukchul, Keesool Gam, Kwangmin Park, Sungpil Ma, and Jinho Lee. "Transient responses of the flat evaporator loop heat pipe." *International Journal of Heat and Mass Transfer* 57, no. 1 (2013): 131-141. https://doi.org/10.1016/j.ijheatmasstransfer.2012.10.025

[13] Wang, Dongdong, Zhichun Liu, Song He, Jinguo Yang, and Wei Liu. "Operational characteristics of a loop heat pipe with a flat evaporator and two primary biporous wicks." *International Journal of Heat and Mass Transfer* 89 (2015): 33-41. https://doi.org/10.1016/j.ijheatmasstransfer.2015.05.042

[14] Xu, Jiayin, Zhiyuan Wang, Hong Xu, and Li Zhang. "Experimental research on the heat performance of a flat copper-water loop heat pipe with different inventories." *Experimental Thermal and Fluid Science* 84 (2017): 110-119. https://doi.org/10.1016/j.expthermflusci.2017.02.003

[15] He, Song, Jing Zhao, Zhi-chun Liu, Wei Tian, Jin-guo Yang, and Wei Liu. "Experimental investigation of loop heat pipe with a large squared evaporator for cooling electronics." *Applied Thermal Engineering* 144 (2018): 383-391. https://doi.org/10.1016/j.applthermaleng.2018.08.075

[16] Anand, A. R., Akhil Jaiswal, Amrit Ambirajan, and Pradip Dutta. "Experimental studies on a miniature loop heat pipe with flat evaporator with various working fluids." *Applied Thermal Engineering* 144 (2018): 495-503. https://doi.org/10.1016/j.applthermaleng.2018.08.092

[17] Zhang, Yixue, Junyu Liu, Longfei Liu, Haolin Jiang, and Tao Luan. "Numerical simulation and analysis of heat leakage reduction in loop heat pipe with carbon fiber capillary wick." *International Journal of Thermal Sciences* 146 (2019): 106100.

[18] Singh, Randeep, Aliakbar Akbarzadeh, Chris Dixon, and Masataka Mochizuki. "Novel design of a miniature loop heat pipe evaporator for electronic cooling." *Journal of Heat Transfer* 129 (2007): 1445-1452. https://doi.org/10.1115/1.2754945

[19] Joung, Wukchul, Taeu Yu, and Jinho Lee. "Experimental study on the loop heat pipe with a planar bifacial wick structure." *International Journal of Heat and Mass Transfer* 51, no. 7-8 (2008): 1573-1581. https://doi.org/10.1016/j.ijheatmasstransfer.2007.07.048

[20] Joung, Wukchul, Taeu Yu, and Jinho Lee. "Experimental study on the operating characteristics of a flat bifacial evaporator loop heat pipe." *International Journal of Heat and Mass Transfer* 53, no. 1-3 (2010): 276-285. https://doi.org/10.1016/j.ijheatmasstransfer.2009.09.031

[21] Maydanik, Yu, S. Vershinin, M. Chernysheva, and S. Yushakova. "Investigation of a compact copper-water loop heap pipe with a flat evaporator." *Applied Thermal Engineering* 31, no. 16 (2011): 3533-3541. https://doi.org/10.1016/j.applthermaleng.2011.07.008

[22] Becker, Suzanne, S. Vershinin, V. Sartre, E. Laurien, Jocelyn Bonjour, and Yu F. Maydanik. "Steady state operation of a copper-water LHP with a flat-oval evaporator." *Applied Thermal Engineering* 31, no. 5 (2011): 686-695. https://doi.org/10.1016/j.applthermaleng.2010.02.005

[23] Zhang, Xianfeng, Jiepeng Huo, and Shuangfeng Wang. "Experimental investigation on temperature oscillation in a miniature loop heat pipe with flat evaporator." *Experimental Thermal and Fluid Science* 37 (2012): 29-36. https://doi.org/10.1016/j.expthermflusci.2011.09.010

[24] Wang, Shuangfeng, Jiepeng Huo, Xianfeng Zhang, and Zirong Lin. "Experimental study on operating parameters of miniature loop heat pipe with flat evaporator." *Applied Thermal Engineering* 40 (2012): 318-325. https://doi.org/10.1016/j.applthermaleng.2012.02.029

[25] Choi, Jeehoon, Wataru Sano, Weijie Zhang, Yuan Yuan, Yunkeun Lee, and Diana-Andra Borca-Tasciuc. "Experimental investigation on sintered porous wicks for miniature loop heat pipe applications." *Experimental Thermal and Fluid Science* 51 (2013): 271-278. https://doi.org/10.1016/j.expthermflusci.2013.08.009

[26] Chernysheva, M. A., S. I. Yushakova, and Y. F. Maydanik. "Effect of external factors on the operating characteristics of a copper-water loop heat pipe." *International Journal of Heat and Mass Transfer* 81 (2015): 297-304. https://doi.org/10.1016/j.ijheatmasstransfer.2014.10.037

[27] Maydanik, Yury F., Vladimir G. Pastukhov, and Mariya A. Chernysheva. "Development and investigation of a miniature copper-acetone loop heat pipe with a flat evaporator." *Journal of Electronics Cooling and Thermal Control* 5, no. 04 (2015): 77-88. https://doi.org/10.4236/jectc.2015.54006

[28] Odagiri, Kimihide, and Hosei Nagano. "Heat transfer characteristics of flat evaporator loop heat pipe under high heat flux condition with different orientations." *Applied Thermal Engineering* 153 (2019): 828-836. https://doi.org/10.1016/j.applthermaleng.2019.02.022

[29] Chuang, Po-Ya Abel. "An Improved Steady-State Model Of Loop Heat Pipes Based On Experimental And Theoretical Analyses." *PhD diss., The Pennsylvania State University*, 2003.

[30] Furukawa, Masao. "Model-based method of theoretical design analysis of a loop heat pipe." *Journal of Thermophysics and Heat Transfer* 20, no. 1 (2006): 111-121. https://doi.org/10.2514/1.14675

[31] Adoni, Abhijit A., Amrit Ambirajan, V. S. Jasvanth, D. Kumar, Pradip Dutta, and K. Srinivasan. "Thermohydraulic modeling of capillary pumped loop and loop heat pipe." *Journal of Thermophysics and Heat Transfer* 21, no. 2 (2007): 410-421. https://doi.org/10.2514/1.26222

[32] Launay, Stéphane, Valérie Sartre, and Jocelyn Bonjour. "Analytical model for characterization of loop heat pipes." *Journal of Thermophysics and Heat Transfer* 22, no. 4 (2008): 623-631. https://doi.org/10.2514/1.37439

[33] Bai, Lizhan, Guiping Lin, Hongxing Zhang, and Dongsheng Wen. "Mathematical modeling of steady-state operation of a loop heat pipe." *Applied Thermal Engineering* 29, no. 13 (2009): 2643-2654. https://doi.org/10.1016/j.applthermaleng.2008.12.040

[34] Singh, Randeep, Aliakbar Akbarzadeh, Chris Dixon, and Masataka Mochizuki. "Theoretical modelling of miniature loop heat pipe." *Heat and Mass Transfer* 46, no. 2 (2009): 209-224.

[35] Chernysheva, Mariya A., and Yury F. Maydanik. "3D-model for heat and mass transfer simulation in flat evaporator of copper-water loop heat pipe." *Applied Thermal Engineering* 33 (2012): 124-134. https://doi.org/10.1016/j.applthermaleng.2011.09.025

[36] Chernysheva, Mariya A., Vladimir G. Pastukhov, and Yury F. Maydanik. "Analysis of heat exchange in the compensation chamber of a loop heat pipe." *Energy* 55 (2013): 253-262. https://doi.org/10.1016/j.energy.2013.04.014

[37] Hamdan, Mohammad, and Emad Elnajjar. "Loop heat pipe: Simple thermodynamic." *World Academy of Science, Engineering and Technology* 52 (2009): 161-167. https://doi.org/10.1007/s00231-009-0555-0

[38] Ghajar, M., and J. Darabi. "Evaporative heat transfer analysis of a micro loop heat pipe with rectangular grooves." *International Journal of Thermal Sciences* 79 (2014): 51-59. https://doi.org/10.1016/j.ijthermalsci.2013.12.014

[39] Lin, Fang-Chou, Bing-Han Liu, Chi-Ting Huang, and Yau-Ming Chen. "Evaporative heat transfer model of a loop heat pipe with bidisperse wick structure." *International Journal of Heat and Mass Transfer* 54, no. 21-22 (2011): 4621-4629. https://doi.org/10.1016/j.ijheatmasstransfer.2011.06.015

[40] Siedel, Benjamin, Valérie Sartre, and Frédéric Lefèvre. "Numerical investigation of the thermohydraulic behaviour of a complete loop heat pipe." *Applied Thermal Engineering* 61, no. 2 (2013): 541-553. https://doi.org/10.1016/j.applthermaleng.2013.08.017

[41] Bai, Lizhan, Guiping Lin, Zuodong Mu, and Dongsheng Wen. "Theoretical analysis of steady-state performance of a loop heat pipe with a novel evaporator." *Applied Thermal Engineering* 64, no. 1-2 (2014): 233-241. https://doi.org/10.1016/j.applthermaleng.2013.12.052

[42] Bai, Lizhan, Jinghui Guo, Guiping Lin, Jiang He, and Dongsheng Wen. "Steady-state modeling and analysis of a loop heat pipe under gravity-assisted operation." *Applied Thermal Engineering* 83 (2015): 88-97. https://doi.org/10.1016/j.applthermaleng.2015.03.014

[43] Zhu, Lin, and Jianlin Yu. "Simulation of steady-state operation of an ejector-assisted loop heat pipe with a flat evaporator for application in electronic cooling." *Applied Thermal Engineering* 95 (2016): 236-246. https://doi.org/10.1016/j.applthermaleng.2015.11.028

[44] Siedel, Benjamin, Valérie Sartre, and Frédéric Lefèvre. "Complete analytical model of a loop heat pipe with a flat evaporator." *International Journal of Thermal Sciences* 89 (2015): 372-386. https://doi.org/10.1016/j.ijthermalsci.2014.11.014

[45] Chernysheva, M. A., and Yu F. Maydanik. "Peculiarities of heat transfer in a flat disk-shaped evaporator of a loop heat pipe." *International Journal of Heat and Mass Transfer* 92 (2016): 1026-1033. https://doi.org/10.1016/j.ijheatmasstransfer.2015.08.108

[46] Esarte, J., A. Bernardini, J. M. Blanco, and R. Sancibrian. "Optimizing the design for a two-phase cooling loop heat pipe: Part A: Numerical model, validation and application to a case study." *Applied Thermal Engineering* 99 (2016): 892-904. https://doi.org/10.1016/j.applthermaleng.2016.01.150

[47] Weng, Chih-Yuan, and Tzong-Shyng Leu. "Two-phase flow pattern based theoretical study of loop heat pipes." *Applied Thermal Engineering* 98 (2016): 228-237. https://doi.org/10.1016/j.applthermaleng.2015.11.124

[48] Pozhilov, Aleksey A., Dmitri K. Zaitsev, Evgueni M. Smirnov, and Aleksander A. Smirnovsky. "Numerical simulation of heat and mass transfer in a 3D model of a loop heat pipe evaporator." *St. Petersburg Polytechnical University Journal: Physics and Mathematics* 3, no. 3 (2017): 210-217.

[49] Ramasamy, Navin Subbaiah, Prem Kumar, Bhimashankar Wangaskar, Sameer Khandekar, and Yuri F. Maydanik. "Miniature ammonia loop heat pipe for terrestrial applications: Experiments and modeling." *International Journal of Thermal Sciences* 124 (2018): 263-278. https://doi.org/10.1016/j.ijthermalsci.2017.10.018

[50] Li, Jian, Fangjun Hong, Rongjian Xie, and Ping Cheng. "Pore scale simulation of evaporation in a porous wick of a loop heat pipe flat evaporator using Lattice Boltzmann method." *International Communications in Heat and Mass Transfer* 102 (2019): 22-33. https://doi.org/10.1016/j.icheatmasstransfer.2019.01.008

[51] Chernysheva, M. A., and Y. F. Maydanik. "Simulation of heat and mass transfer in a cylindrical evaporator of a loop heat pipe." *International Journal of Heat and Mass Transfer* 131 (2019): 442-449. https://doi.org/10.1016/j.ijheatmasstransfer.2018.11.034

[52] Gabsi, I., Samah Maalej, and Mohamed Chaker Zaghdoudi. "Thermal performance modeling of loop heat pipes with flat evaporator for electronics cooling." *Microelectronics Reliability* 84 (2018): 37-47. https://doi.org/10.1016/j.microrel.2018.02.023

[53] Chernysheva, M. A., S. I. Yushakova, and Yu F. Maydanik. "Copper-water loop heat pipes for energy-efficient cooling systems of supercomputers." *Energy* 69 (2014): 534-542. https://doi.org/10.1016/j.energy.2014.03.048